

STUDY OF PRASEODYMIUM STRONTIUM MANGANITE FOR THE POTENTIAL  
USE AS A SOLID OXIDE FUEL CELL CATHODE

by

Matthew Edward Pfluge

A thesis submitted in partial fulfillment  
of the requirements for the degree

of

Master of Science

in

Chemical Engineering

MONTANA STATE UNIVERSITY  
Bozeman, Montana

April 2005

©COPYRIGHT

by

Matthew Edward Pfluge

2005

All Rights Reserved

APPROVAL

of a thesis submitted by

Matthew Edward Pfluge

This thesis has been read by each member of the thesis committee and has been found to be satisfactory regarding content, English usage, format, citations, bibliographical style, and consistency, and is ready for submission to the College of Graduate Studies.

Dr. Max Deibert

Approved for the Department of Chemical Engineering

Dr. Ron Larsen

Approved for the College of Graduate Studies

Dr. Bruce McLeod

STATEMENT OF PERMISSION TO USE

In presenting this thesis in partial fulfillment of the requirements for a master's degree at Montana State University, I agree that the Library shall make it available to borrowers under the rules of the Library.

If I have indicated my intention to copyright this thesis by including a copyright notice page, copying is allowable only for scholarly purposes, consistent with "fair use" as prescribed in the U.S. Copyright Law. Requests for permission for extended quotation from or reproduction of this thesis in whole or in parts may be granted only by the copyright holder.

Matthew Edward Pfluge

April 14, 2005

## ACKNOWLEDGEMENTS

I would like to personally thank all of the researchers at Pacific Northwest National Lab that helped me through my journey especially Greg Coffey, Pete Rieke, Larry Pedersen, Ed Thomsen, Carolyn Nguyen, Kerry Meinhardt, Steve Simner, Mike Anderson, and Doug Conner. I would also like to thank my advisors, Dr. Max Deibert and Dr. Dick Smith for their support and always challenging me. I would also like to acknowledge the organizations that provided funding and made this possible including PNNL, SECA, DOE, and specifically the Office of Fossil Energy Advanced Research and Technology Development Materials Program. Finally, I would like to thank my family for their love and support, and Michelle for keeping me going.

## TABLE OF CONTENTS

1. INTRODUCTION .....	1
2. BACKGROUND AND LITERATURE REVIEW .....	2
Solid Oxide Fuel Cells (SOFC).....	2
SOFC Basics .....	2
Decreasing SOFC Operating Temperature .....	5
SOFC Cathode.....	7
Mixed Conductor Theory and Modeling.....	8
Perovskite Structure .....	8
“A” Site Deficiency Importance .....	10
Influence of Doping .....	11
Relevant Cathode Systems .....	12
LaSrMnO <sub>3</sub> .....	12
PrSrMnO <sub>3</sub> .....	14
3. EXPERIMENTAL PROCEDURES .....	17
Glycine-Nitrate Pyrolysis .....	17
Sample Preparation.....	20
Calcination .....	20
Attrition Milling.....	20
Ink Preparation .....	21
Pellet and Bar Pressing.....	21
XRD Evaluation .....	22
Phase Purity.....	22
Archimedes Density .....	23
Dilatometry .....	23
Electronic Conductivity.....	24
Ionic Conductivity .....	25
Seebeck Measurements.....	26
Half – Cell Measurements .....	27
4. RESULTS AND DISCUSSION .....	29
XRD Evaluation .....	29
Phase Purity Peaks .....	29
Relative Density .....	31
Dilatometry .....	32
Sintering Study .....	32
TEC Calculation.....	33
Analysis.....	34

## TABLE OF CONTENTS CONTINUED

Electronic Conductivity .....	35
Calculations .....	35
Analysis .....	38
Ionic Conductivity .....	39
Calculations .....	39
Analysis .....	40
Seebeck Measurements.....	41
Calculations .....	41
Analysis .....	42
Half – Cell Measurements .....	43
Calculations .....	43
Analysis .....	52
5. CONCLUSIONS AND RECOMMENDATIONS .....	54
SOURCES CITED.....	56

## LIST OF TABLES

Table	Page
1: PSM compositions and nitrate solutions for glycine-nitrate combustion. ....	18
2: Sample mass calculations for nitrate solution and glycine. ....	19
3: Relative and percent densities calculations .....	31
4: Tabulated values of chemical reaction constants and area specific resistance throughout the cathode layer. ....	46

## LIST OF FIGURES

Figure	Page
2.1 Schematic of Solid Oxide Fuel Cell [4].	4
2.2 $ABO_3$ perovskite structure.	10
3.1 Sample used for the four-point AC conductivity experiments.	24
3.2 Oxygen permeation assembly.	25
3.3 Assembly structure for Seebeck coefficient measurements.	26
3.4 Half-cell measurement set-up.	27
4.1 XRD phase peaks for the PSM data set with references for silicon, PSM and Hausmannite.	30
4.2 Densification Study of samples up to 1400°C.	33
4.3 TEC measurements of sample set with comparison to common electrolyte and anode material.	34
4.4 Electrical conductivity measurement from 200°C to 950°C.	36
4.5 Arrhenius plot of electrical conductivity measurement.	37
4.6 Activation energies for electrical conductivity.	38
4.7 Oxygen permeation from 200°C to 950°C.	40
4.8 Seebeck measurements for the sample set from 100°C to 950°C.	41
4.9 Half cell measurement for sample set at 850°C in air.	44
4.10 Example of hyperbolic sine curve fit to PSM 10 data at 850°C.	45
4.11 PSM 10 half cell after testing.	47
4.12 PSM 20 half cell after testing.	48
4.13 PSM 20A half cell after testing.	49
4.14 PSM 30 half cell after testing.	50
4.15 PSM 30A half cell after testing.	51

## ABSTRACT

Extensive research has been performed on solid oxide fuel cell cathodes. These cathodes must be stable in the oxidation environment and have sufficient electrical conductivity and catalytic activity for the oxidant gas reaction at the appropriate operating temperature. Also, the cathode must be chemically and thermally compatible with the other cell components at room temperature, operating temperatures, and higher fabrication temperatures. Praseodymium strontium manganite (PSM) has shown promising electrical properties with respect to ideal properties of cathodes in solid oxide fuel cells. Various dopant levels of strontium in the perovskite structure were investigated, which include  $\text{Pr}_{1-x}\text{Sr}_x\text{MnO}_{3-\delta}$  where  $x = 0.10, 0.20, 0.30$  and  $(\text{Pr}_{1-x}\text{Sr}_x)_{0.98}\text{MnO}_{3-\delta}$  where  $x = 0.20$  and  $0.30$ . This cathodic material has shown electrical conductivity over twice as high as a traditionally used cathode,  $\text{La}_{0.8}\text{Sr}_{0.2}\text{MnO}_3$ . Through this investigation, the electrical and ionic conductivities of this ceramic series were measured from  $200^\circ\text{C}$  to  $950^\circ\text{C}$ . Another important electrical measurement investigated was the Seebeck coefficient within the same temperature range. This coefficient is a measurement of the change in voltage across a temperature gradient and thus can be referred to as its thermal power. Conductor types have been interpolated from the measurements. This measurement provides an improved understanding of the high electrical properties displayed within the material. Cathodic overpotential was also measured using half cell reactions performed in the temperature range of  $650^\circ\text{C}$  to  $850^\circ\text{C}$  under both air and pure oxygen. This measurement was used to calculate the current exchange density of the cathode and the area specific resistance. Overall, as the strontium concentration increased, the electrical activity of the ceramic subsequently increased. Furthermore, in relation to the traditional cathode material,  $\text{La}_{0.8}\text{Sr}_{0.2}\text{MnO}_3$ , the substitution of lanthanum with praseodymium has produced more effective cathodic performance.

## CHAPTER 1

## INTRODUCTION

Solid oxide fuel cells (SOFC) have been studied extensively for a broad spectrum of electrical power generation applications because of their clean and efficient electrical energy production. The potential for these fuel cells is immense and they promise to be an important alternative energy source for a less oil dependant future.

Technological developments of this promising energy source are in their developmental stage with copious challenges left to be resolved before the SOFC fuel cell can be fully utilized. SOFC technology has recently received vast amounts of funding originating from the Department of Energy resulting in advances in ceramic technology, engineering material compositions, testing methods, property relationships, and processing intricate matrices. Additionally, this research, conducted through the Department of Energy, has sparked further advances in ceramic synthesis, characterization, and other properties.

## CHAPTER 2

## BACKGROUND AND LITERATURE REVIEW

Solid Oxide Fuel Cells (SOFC)SOFC Basics

Solid oxide fuel cells are prominent candidates for power generation that convert chemical energy directly to electricity with high efficiency and little pollution. This device bypasses the conversion of the chemical energy of the fuel into thermal and mechanical energy which leads to losses and therefore achieves a theoretical efficiency significantly higher than that of conventional power generation methods. This efficiency is around 45% to 60% and may achieve an even higher efficiency if the byproduct heat is fully utilized in the system [1].

Fuel cells have many advantages over conventional power generators. Fuel cells are more versatile than conventional mechanical power generation devices, and they can be increased and decreased in size for a variety of applications relevant to different power needs [2]. Furthermore, the efficiency of the fuel cell is independent of size and can be designed to follow loads with fast response times. The fuel cell's operation is, in addition, quiet because of the lack of moving parts; therefore, fuel cells can be located anywhere, including within residential areas. Another advantage of fuel cells is the fact that they are environmentally friendly devices, especially considering fuel cells are

capable of using a variety of different fuels with minute environmental impacts. Emissions of pollutants like  $\text{NO}_x$ ,  $\text{SO}_x$ , and dangerous particulates from fuel cells are far lower than those from conventional power generators [1]. Certain high temperature fuel cells like SOFCs also have a multifuel capability. Since these fuel cells are operated at an elevated temperature, they can process hydrocarbon fuels internally through reforming reactions and do not need expensive subsystems to process these fuels. It is this particular capability of the fuel cell that will likely facilitate a transition from conventional fuel sources like gasoline and natural gas to strictly hydrogen gas [1].

The main distinction among ceramic fuel cells is a solid ceramic material that conducts ions without electrical conduction called the electrolyte with two ceramic electrodes attached on either side of this electrolyte, one being the cathode while the other is the anode. The ionic permeation requirement through this ceramic electrolyte necessitates a high operating temperature from  $600^\circ\text{C}$  to  $1000^\circ\text{C}$  [3]. These intense temperatures promote rapid reaction kinetics, allow reforming of hydrocarbon fuels, and generate byproduct heat. However, stringent material restrictions and processing requirements required by these extreme temperatures prove to be a disadvantage of SOFCs.

A schematic of a solid oxide fuel cell is shown in figure 2.1.

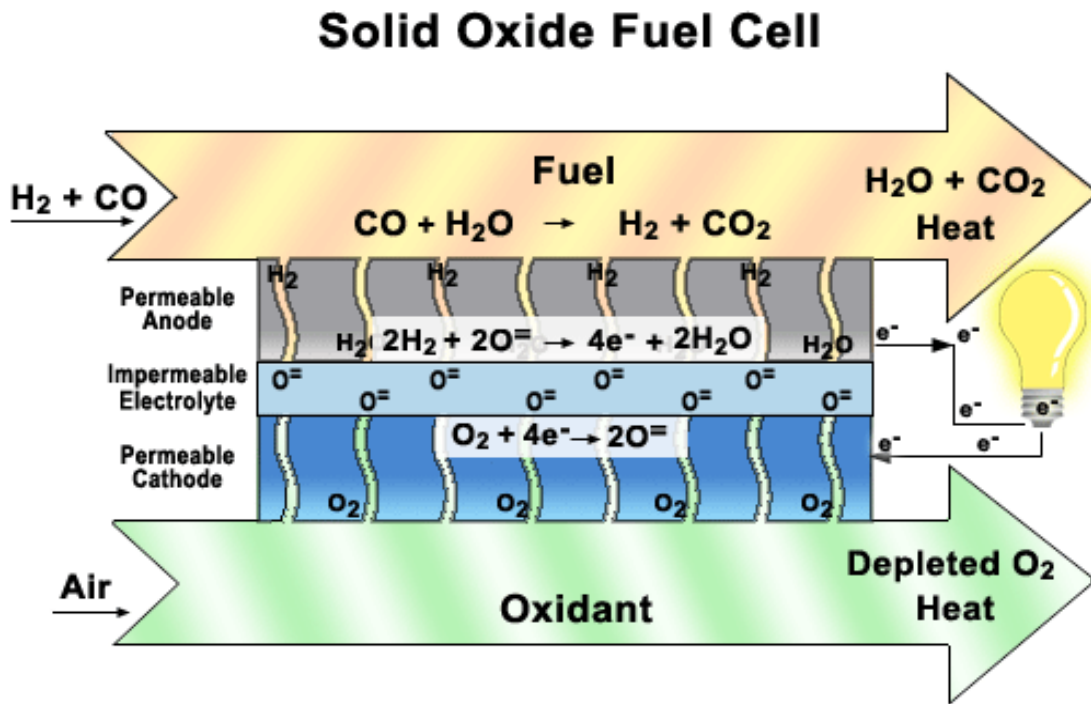
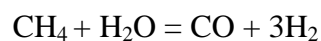
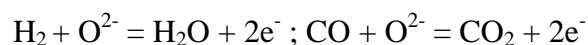


Figure 2.1: Schematic of Solid Oxide Fuel Cell [4].

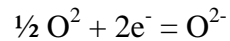
A solid oxide fuel cell consists of a solid ceramic electrolyte surrounded by two ceramic electrodes: a cathode and an anode. Fuel is fed on the anode side and undergoes an oxidation reaction while releasing electrons to an external circuit. Air or pure oxygen is fed to the cathode side where it undergoes a reduction reaction and accepts the electrons from the circuit. This electron flow produces direct current electricity. The solid electrolyte conducts oxygen ions from the cathode to the anode to complete the electrochemical process. If methane is fed to the anode side, it is steam reformed by:



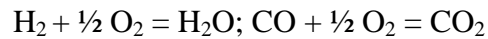
The reactions on the anode side are:



The reaction on the cathode side is:



Therefore, the overall reactions for the fuel cell are:



Therefore, the SOFC is considered to be an oxygen dilution cell, so the reversible open circuit voltage for the fuel cell is given by the Nernst equation [1]:

$$E_r = \frac{R \cdot T}{4 \cdot F} \cdot \ln \left( \frac{P_{\text{O}_2(\text{c})}}{P_{\text{O}_2(\text{a})}} \right)$$

where R is the gas constant, T the temperature, F the Faraday's constant, and  $P_{\text{O}_2}$  the partial pressure of oxygen at the electrode. The overall cell voltage can be described by:

$$V = E_r - iR - \eta_a - \eta_c$$

where  $iR$  is the ohmic resistance,  $\eta_a$ ,  $\eta_c$  are the anode and cathode polarizations [5].

### Decreasing SOFC Operating Temperature

Currently, the operating temperature of a solid oxide fuel cell is around 1000°C; however, many limitations occur at such a high temperature. Chemical instabilities among different cell components develop, along with the diffusion of different elements throughout the ceramic matrix from individual components into adjacent components [6]. Porous ceramic electrodes densify at these high operating temperatures, which decreases the oxygen flux on the cathode side and the flux of fuel gas on the anode side toward the electrolyte. This drastically decreases the overall performance of the fuel cell [7]. Also, the individual cell components experience delamination due to slight differences in the

thermal expansion coefficient and the extreme thermal cycling experienced by the fuel cell. Finally, the largest limitation of high operating temperatures is the fact that the interconnect and manifolding materials required at these temperatures become the most expensive components of the fuel cell [1].

Considering all of the disadvantages of the high operating temperature, it is evident that research is needed in order to decrease the temperature to 650°C to 750°C [5]. With such an alteration in temperature, the lifetime of the fuel cell is greatly increased due to decreased interactions of the electrodes and the electrolyte. Ferritic stainless steels can be used for the interconnect material, which are less expensive raw materials and have lower manufacturing costs than the traditional ceramic lanthanum strontium chromite interconnect. The manifolding material is also less costly. Also, the startup time for the SOFC is significantly less [1].

With all of the advantages of decreasing the operating temperatures, the transition seems to be inevitable; however, many challenges must be overcome. Oxygen permeation and electrical conductivities are thermally activated and significantly increase with rising temperatures. Oxygen ionic conductivity through the electrolyte exponentially decreases, increasing the overall cell resistance. An additional source of performance loss is in the charge transfer polarization of electrodes. To combat these challenges, the electrodes need to have a higher electrical and ionic conductivity. Furthermore, these electrodes need to have a fine grain size and higher porosity to increase the number of sites for charge transfer reactions. All components need to be manufactured thinner to decrease the ohmic resistance throughout the fuel cell [1-7].

### SOFC Cathode

The main function of the cathode is to provide reaction sites for the electrochemical reduction of the oxidant,  $O_2$ . The cathode must be stable in the oxidation environment and have sufficient electrical conductivity and catalytic activity for the oxidant gas reaction at the appropriate operating temperature. Also, the cathode must be chemically and thermally compatible with the other cell components from room temperature to the operating temperature and to even higher fabrication temperatures [8].

The cathode has to be chemically, morphologically, and dimensionally stable in an oxidant environment. It can not have disruptive phase transformations throughout the temperature range from room temperature to the operating temperature. In addition, the desired microstructure must be maintained in long-term operation because significant changes can degrade the performance of the fuel cell [1].

Electrical conductivity of the cathode must support significant electron flow to the reaction sites at the interface of the electrolyte and cathode in the oxidizing environment at the operating temperature. Maximum conductivity correlates to a minimization of ohmic losses throughout the fuel cell. Ionic conductivity of the cathode is important as well. The ability of the cathode to conduct oxygen ions provides more oxygen sites to the electrolyte interface, which will improve the overall performance of the fuel cell.

Compatibility of the cathode with other components is another important aspect of its development. Chemical reactions and elemental interdiffusion between the cathode and adjoining components needs to be limited or completely eliminated to minimize

second phase formations, stability reduction, change in thermal expansion, enhanced electrical conductivity of the electrolyte and elimination of ionic conductivity in the electrolyte among other effects [1].

The thermal expansion coefficient of the cathode needs to match all other cell components from room temperature to the operating temperatures. This will avoid cracking and delamination during fabrication and operating with thermal cycling.

The cathode needs to have sufficient porosity to allow oxidant gas transport to the reaction sites near the cathode-electrolyte interface. The lower limit on porosity is based on the mass transport of the oxidant gas, while the upper limit is based on mechanical strength of the component. There needs to be sufficient contact area of the cathode to the electrolyte to provide enough reaction sites and enough porosity to supply sufficient oxidant gas transport.

A combination of these essential requirements should correlate to the catalytic activity of the cathode. Other desirable properties are high strength and toughness, ease of fabrication, and ultimately a low cost. Electronic or mixed conducting oxides are the best suited for the cathodic duties.

### Mixed Conductor Theory and Modeling

#### Perovskite Structure

Most mixed conducting ceramic materials have the most desirable properties for a SOFC while in the perovskite structure. This structure is named from the mineral

perovskite, which has a chemical formula of  $\text{CaTiO}_3$  and is a naturally occurring mineral that is abundant in chlorite, talc, and serpentine rocks. However, in this case, the term perovskite refers to the  $\text{ABO}_3$  structure that is used for a wide variety of mixed conductor systems. The  $\text{ABO}_3$  perovskite structure has technological applications that make use of this structure's ability to form oxygen vacancies with proper amounts of doping ions with differing oxidation states. This is due to perovskites having large tolerances for departure from ideal stoichiometry [3].

The principal perovskite structure is cubic containing three distinct sites for ions: A, B, and O, shown in figure 2.2. The A and B atoms represent cations, while the O refers to the oxygen anion with a negative 2 charge. In general terms, the  $\text{ABO}_3$  structure can be described as face-centered cubic with A atoms at the corners, O atoms on the faces, and a B atom occupying the octahedral site in the center. The largest of the cations is the A site cation.

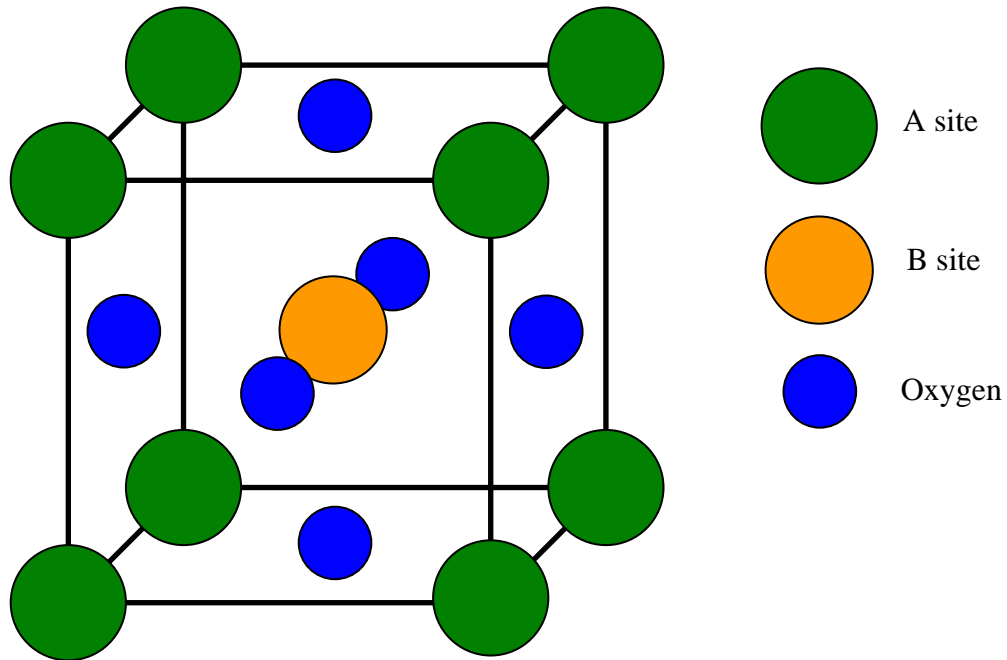


Figure 2.1:  $ABO_3$  perovskite structure.

### “A” Site Deficiency Importance

In figure 2.2, a typical perovskite structure is shown. Using Pr and Sr as A site atoms and Mn as the B site atom, the A site atoms, especially Pr atoms, are larger than the Mn atoms in the B site. This means that the A site atoms dominate the overall crystalline structure. Considering perovskite structure consisting of more A site atoms than B site, the larger A site atoms will expand the crystalline structure in the direction of the Pr atoms, which will deform and construe the structure creating a non-cubic or non-ideal structure. In order to eliminate this phenomenon, a B site rich or A site deficient structure is created. Therefore, the effects of a 2% A site deficiency were studied.

### Influence of Doping

The ability of the perovskite structure to tolerate changes in its stoichiometry means that the material can be altered by the substitution of different cations in the A and B sites. Several functional properties of a perovskite can be modified by the total or partial replacement of the A and B site cations. Since mixed conductors are candidates for structures that require large amounts of ionic conductivity, one of the more frequent reasons for doping a material with ions with differing oxidation states is to increase the ionic conductivity. One of the most common methods of doing this is an A-site substitution to facilitate the formation of oxygen vacancies [3].

Transition metals are normally used for the B site atoms as they can assume a mixed-valence state. The partial substitution of the A site cations by other metal cations with lower valence states can cause the formation of oxygen vacancies. This is accompanied by a decrease in the B site cation valence states. This allows the material to maintain charge neutrality [10]:

$$[A'_A] = [B^*_B] + [V_{O}^{\bullet\bullet}]$$

where  $A'_A$  refers to doping the A site with a cation with one less positive valence state,  $B^*_B$  refers to the B site cation increasing one valence charge and  $V_{O}^{\bullet\bullet}$  refers to the formation of an oxygen vacancy. The Kroger-Vink notation, where the brackets indicate concentrations of the indicated species, is utilized in this equation. The equation means that for every substitution made into the A site, where the new cation has a valence one less than the original cation, there must be a compensation for the charge difference created by this substitution. The compensation can either come from an increase in the

valence of the B site cations (electronic compensation) or the formation of oxygen vacancies (ionic compensation) [8]. This increase in oxygen vacancy population leads to an increase in ionic conductivity.

### Relevant Cathode Systems

#### LaSrMnO<sub>3</sub>

The La<sub>1-x</sub>Sr<sub>x</sub>MnO<sub>3-δ</sub> (LSM) system is the most commonly used cathode material for SOFCs. Under normal operating conditions, LSM exhibits a negligible amount of ionic conductivity, which limits the cathode reaction to the triple-phase boundary where the cathode, electrolyte and oxygen are all in contact [6, 7, 9-21]. The electrical conductivity of this material is acceptable at the operating temperatures of the SOFC; however, increasing these conductivities (electrical and ionic) would decrease the electrode polarization and subsequently increase the fuel cell's performance [11]. The major setback of the LSM system is that the cathode and the yttria-stabilized zirconia (YSZ) electrolyte form highly resistant products, such as La<sub>2</sub>Zr<sub>2</sub>O<sub>7</sub> at high temperatures [12]. This reaction greatly reduces the fuel cell performance and the lifetime of such a cell.

At SOFC operating temperatures, LSM is stable in oxidizing atmospheres but decomposes under highly reducing conditions. LSM decomposes directly to La<sub>2</sub>O<sub>3</sub> and MnO at critical oxygen partial pressures of about 10<sup>-14</sup> to 10<sup>-15</sup> atm at temperatures above 1100°C [11]. At lower temperatures from 350°C to 600°C, this cathode tends to

transform to other phases such as  $\text{La}_2\text{MnO}_4$ ,  $\text{La}_4\text{Mn}_4\text{O}_{11}$ ,  $\text{La}_8\text{Mn}_8\text{O}_{23}$ , and  $\text{SrMnO}_3$  [14]. Nonstoichiometry has an influence on the stability of LSM. Lanthanum excess can precipitate into  $\text{La}_2\text{O}_3$  formation; however, lanthanum deficiencies can lead to  $\text{Mn}_3\text{O}_4$  formations. The lanthanum deficiency should not exceed 10% throughout the matrix [6-7].

LSM is an intrinsic p-type electrical conductor due to the formation of cation vacancies. The electrical conductivity of LSM takes place via small polaron hopping throughout the ceramic matrix [7]. (A polaron is defined as an electron that travels through a solid state material that, as it passes by positive ions, attracts them and, as it passes by negative ions, repels them. This electronic transport deforms the overall structure slightly as electrons pass through the structure.) The electrical conductivity of LSM increases with increasing temperature and increasing strontium concentration. The conductivity increases from 130 S/cm to 290 S/cm at 1000°C when the strontium concentration is increased from 10% to 50% [1].

The chemical reactions of LSM and YSZ have been extensively studied at SOFC operating and fabricating temperatures. Above 1200°C,  $\text{La}_2\text{Zr}_2\text{O}_7$  is produced and a layer 5  $\mu\text{m}$  thick can form at the LSM/YSZ interface if sintered at 1450°C for 48 hr [7]. With high strontium dopant concentration (above 40%),  $\text{SrZrO}_3$  is formed, and with strontium concentrations from 20% to 50%,  $\text{La}_2\text{Zr}_2\text{O}_7$  and  $\text{SrZrO}_3$  are formed at temperatures above 1400°C [6]. The formations of these phases are undesirable and detrimental to the performance of the solid oxide fuel cell. These phases act as an insulating layer and create thermal stresses at the interface. The thermal expansion coefficients of these

phases are significantly lower than that of YSZ and LSM and therefore will create undesirable stresses at the cathode-electrolyte interface. These stresses can cause delamination which can lead to severe cracking within the entire fuel cell plate [1].

### PrSrMnO<sub>3</sub>

The Pr<sub>1-x</sub>Sr<sub>x</sub>MnO<sub>3-δ</sub> (PSM) system has been studied by many as a candidate for an alternative cathode for the SOFC [23-28]. Praseodymium's ion size is slightly greater than lanthanum's, which could have an impact on the perovskite structure. This means that an excess of Pr could have more of impact than an excess of La on the cathodic performance. However, at high temperatures Pr changes oxidation states from Pr<sup>+3</sup> to Pr<sup>+4</sup>; this should increase the electrical conductivity of the ceramic and lower the cathodic overpotential because La consists of only one oxidation state of La<sup>+3</sup> [22]. Therefore, the replacement of La with Pr should increase the overall cathodic performance, which is shown in recent research. Electrical conductivity measurements and cathodic overpotential for the PSM system have been reported much better than the traditional cathode material, LSM. In recent studies, Pr deficiencies in the overall structure have been emphasized in the research [23-28].

X. Huang et al. have reported research on Pr<sub>0.6-x</sub>Sr<sub>0.4</sub>MnO<sub>3</sub> with x = 0, 0.01, 0.05, 0.1, 0.15, and 0.2 [23]. The XRD results of this system show that the main structure is perovskite with small impurities of SrMn<sub>3</sub>O<sub>6-δ</sub> and Pr<sub>6</sub>O<sub>11</sub>. Similar to the LSM system, The Pr<sub>6</sub>O<sub>11</sub> phase results from an excess of Pr, when x is 0.01 and 0. The SrMn<sub>3</sub>O<sub>6-</sub>

$\delta$  phase is evident as  $x$  increased and resulted from an excess of Sr and Mn ions. Therefore, some Pr deficiency can produce a single phase perovskite structure.

The electrical conductivity of this system increased with an increase in Pr deficiency. This seems to represent an increase in mobility and concentration of the polarons as Pr deficiencies increased. At 750°C, the maximum conductivity was measured at 121.7 S/cm when  $x = 0.05$ . With the formation of  $\text{SrMn}_3\text{O}_{6-\delta}$  phase, the electrical conductivity decreased because this phase's conductivity is about 25 times less than that of the single phase perovskite PSM structure. The PSM set measured a higher conductivity than a similar LSM system, which suggests replacing La with Pr increases the electrical conductivity. The cathodic overpotential for this system was lower than the LSM system, with Pr deficiency lowering this value, and  $x = 0.05$  produced the lowest cathodic overpotential [23].

H. Ullman et al. reported results for  $\text{Pr}_{0.65}\text{Sr}_{0.3}\text{MnO}_3$ ,  $\text{Pr}_{0.7}\text{Sr}_{0.3}\text{MnO}_3$ , and  $\text{Pr}_{0.8}\text{Sr}_{0.2}\text{MnO}_3$  ceramics. Using XRD analysis, it was shown that this ceramic developed into a perovskite structure after being sintered at 1450°C for 20 hours. The thermal expansion coefficient  $\text{Pr}_{0.65}\text{Sr}_{0.3}\text{MnO}_3$  was measured at  $11.6 * 10^{-6}\text{K}^{-1}$ , which is close to the values of the commonly used YSZ electrolyte and Ni-YSZ anode. The electrical conductivities of the system were also measured. As the Sr concentration increased, the conductivity also increased with  $\text{Pr}_{0.65}\text{Sr}_{0.3}\text{MnO}_3$  being the highest. The ionic conductivity was also measured, demonstrating that the substitution of La with Pr did not influence oxygen permeation. Therefore, the oxygen permeation throughout this system

is negligible but should be further investigated because maximizing the ionic conductivity would lead to more effective cathode performance [27].

## CHAPTER 3

## EXPERIMENTAL PROCEDURES

Glycine-Nitrate Pyrolysis

Five compositions of  $\text{Pr}_{1-x}\text{Sr}_x\text{MnO}_{3-\delta}$  where  $x = 0.10, 0.20, 0.30$  and  $(\text{Pr}_{1-x}\text{Sr}_x)_{0.98}\text{MnO}_{3-\delta}$  where  $x = 0.20$  and  $0.30$  were created using a glycine-nitrate pyrolysis process. The appropriate amounts of praseodymium, strontium and manganese nitrate salts were mixed together in a large glass beaker to obtain the desired compositions. The concentrations of these nitrate salts were determined using either a gravimetric or compleximetric titration.

The gravimetric method is the simpler of the two methods, but may only be performed on the nitrate salt concentrations if the element of interest has only one-valence state, like praseodymium (+3) and strontium (+2) at lower temperatures. For the manganese nitrate salt, compleximetric titration was utilized to obtain the concentration. Once the aqueous nitrate salts are mixed, glycine powder was added to the solution at twice the stoichiometric quantity to complete the glycine-nitrate combustion reaction. The nitrate salts and glycine are stirred together until the glycine is completely dissolved.

In the tables below, sample calculations for the mass of nitrate salt and mass of glycine powder can be found, along with a table of all of the masses mixed in order to obtain the correct ceramic composition. In a tall stainless steel pot, 100 mL of the

glycine-nitrate solution is added and placed on a hot plate inside of a fume hood, while the remaining solution is continuously stirred. Because of the tall height of the pot and the small amount of liquid being used, the solution does not boil over. The water in the solution is allowed to boil away to concentrate the nitrates and glycine. Once the solution is concentrated, the glycine reacts with the nitrates in an exothermic reaction reaching temperatures above 1200°C [26]. This reaction's products include an oxide ceramic powder in the form of ash, with byproducts of nitrogen, oxygen, water and carbon dioxide gases, and heat. The ash is collected from the bottom of the pot and another 100 mL of solution is added to the pot to begin the process again until no solution remains.

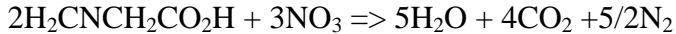
Table 1: PSM compositions and nitrate solutions for glycine-nitrate combustion.

Compositions	Pr(NO <sub>3</sub> ) <sub>3</sub> 0.457 mol/kg	Sr(NO <sub>3</sub> ) <sub>2</sub> 2.0254 mol/kg	Mn(NO <sub>3</sub> ) <sub>2</sub> 1.163 mol/kg	Glycine
Pr <sub>0.9</sub> Sr <sub>0.1</sub> MnO <sub>3-δ</sub> PSM 10	1969.37 grams	49.37 grams	859.84 grams	390.36 grams
Pr <sub>0.8</sub> Sr <sub>0.2</sub> MnO <sub>3-δ</sub> PSM 20	1750.55 grams	98.75 grams	859.84 grams	380.35 grams
Pr <sub>0.7</sub> Sr <sub>0.3</sub> MnO <sub>3-δ</sub> PSM 30	1531.73 grams	148.12 grams	859.84 grams	370.35 grams
(Pr <sub>0.8</sub> Sr <sub>0.2</sub> ) <sub>0.98</sub> MnO <sub>3-δ</sub> PSM 20 A	1715.53 grams	96.77 grams	859.84 grams	374.75 grams
(Pr <sub>0.7</sub> Sr <sub>0.3</sub> ) <sub>0.98</sub> MnO <sub>3-δ</sub> PSM 30 A	1501.09 grams	145.16 grams	859.84 grams	364.94 grams

Table 2: Sample mass calculations for nitrate solution and glycine.

Sample Calculations of the mass of nitrate salts used in the glycine-nitrate pyrolysis to create 1 mol of PSM 10		
$N_{Pr} := 0.9 \text{ mol}$	$C_{PrNO_3} := 0.457 \frac{\text{mol}}{\text{kg}}$	Nitrate salt concentrations were calculated using gravimetric or titration methods.
$N_{Sr} := 0.1 \text{ mol}$	$C_{SrNO_3} := 2.0254 \frac{\text{mol}}{\text{kg}}$	
$N_{Mn} := 1 \text{ mol}$	$C_{MnNO_3} := 1.163 \frac{\text{mol}}{\text{kg}}$	
Calculation to determine mass of nitrate salts used in combustion reaction		
$M_{PrNO_3} := \frac{N_{Pr}}{C_{PrNO_3}}$		$M_{PrNO_3} = 1969.37 \text{ gm}$
$M_{SrNO_3} := \frac{N_{Sr}}{C_{SrNO_3}}$		$M_{SrNO_3} = 49.37 \text{ gm}$
$M_{MnNO_3} := \frac{N_{Mn}}{C_{MnNO_3}}$		$M_{MnNO_3} = 859.85 \text{ gm}$
Calculation of the mass of fuel or glycine supplied to the reaction		
$Pr := 3$	Moles of nitrates in 1 mol of individual nitrate salt	
$Sr := 2$		
$Mn := 2$		
$N_{PrNO_3} := N_{Pr} \cdot Pr$	$N_{SrNO_3} := N_{Sr} \cdot Sr$	$N_{MnNO_3} := N_{Mn} \cdot Mn$
$N_{Total\_NO_3} := N_{PrNO_3} + N_{SrNO_3} + N_{MnNO_3}$		$N_{Total\_NO_3} = 4.9 \text{ mol}$
Formation of 1 mol of PSM 10 requires 3 moles of oxygen atoms, where 1 mol of NO <sub>3</sub> supplies 3 oxygen atoms		
$N_{consumed} := N_{Total\_NO_3} - 1 \text{ mol}$		$N_{consumed} = 3.9 \text{ mol}$
According to the glycine combustion reaction, every 2 moles of glycine reacts with 3 moles of NO <sub>3</sub>		
$\rho_{\text{glycine}} := 75.04 \frac{\text{gm}}{\text{mol}}$		$M_{\text{glycine}} := \frac{2}{3} N_{consumed} \cdot \rho_{\text{glycine}}$
$M_{\text{glycine}} = 195.1 \text{ gm}$		Mass of glycine for stoichiometric reaction
Twice this mass of glycine was mixed to create reducing conditions for this reaction		

The glycine-nitrate reaction is [29]:



### Sample Preparation

#### Calcination

The first step after the reaction is to sieve the powder produced through glycine pyrolysis through a 45- $\mu\text{m}$ -sieve tray, so that the particle sizes are relatively uniform before calcination begins. The powder is carefully poured into crucibles and covered to prevent ceramic powder contamination in the furnace. These powders were heated to 1200°C for two hours using a heating and cooling rate of three degrees per minute. This calcination step is intended to drive any nitrates, excess oxygen and impurities out of the powder and induces a single-phase ceramic crystalline structure. The powder densifies to approximately 30% its original volume and occasionally needs to be ground back down to powder after calcination using mortar and pestle.

#### Attrition Milling

The calcined powder is first sieved through the 45- $\mu\text{m}$ -sieve tray and is then weighed. Isopropanol is measured to half the mass of the ceramic powder. In the attrition-milling canister, half of the alumina beads being used are added, then the ceramic powder is added, next the isopropanol, and finally the rest of the alumina beads. This canister is attached to the attrition-milling machine and left on for two hours. The

purpose of this step is to grind the particulate powder to a size under a micron. This is essential for the particles to adhere well to the YSZ electrolyte for half-cell testing. After attrition milling, a small sample is analyzed in a particle size analyzer to ensure the particle size is under a micron and is relatively uniform.

### Ink Preparation

For half-cell testing, an YSZ electrolyte pellet is screen printed with cathodic ink. This ink is prepared by measuring 10 grams of the calcined powders and mixing it with 5.38 grams of screen print binder Ferro binder B-75717. This binder consists of a polymeric material, polyvinyl buytral, with a carbitol acetate solvent. This binder completely decomposes at 350°C in an air atmosphere with adequate airflow. The weight percent of powder to binder gives a 65% solids loading in the prepared ink. Once the powder and binder are thoroughly mixed together, the mixture is added to a three-roll mill (Exakt 11671 three-roll mill) and rolled through twice. The three-roll mill is used to thoroughly mix the powder and binder together so that each ceramic particle is thoroughly coated with the screen print binder. The ink is then put into jars and labeled accordingly.

### Pellet and Bar Pressing

Some of the calcined powder is pressed into rectangular bars 4.5 cm in length and 1.6 cm wide for electrical conductivity, Seebeck, and dilatometry measurements. Some of the calcined powder can also be pressed into circular pellets of a diameter of 3.2 cm

for oxygen permeation measurements. For a rectangular bar, 7 grams of powder are weighed out and evenly distributed throughout the dye and pressed with the top part of the dye, using uniaxial pressure of about 6 MPa, followed by cold isostatic pressing above 500 MPa. For the circular pellet, 5 grams of powder are measured and again evenly distributed throughout the dye and gently pressed to the top of the dye. It is pressed using uniaxial pressure of about 2 MPa, followed by cold isostatic pressing above 500 MPa. These bars and pellets are then sintered to densify and add tensile strength to the piece before testing.

### XRD Evaluation

#### Phase Purity

Phase purity was determined by x-ray diffraction (XRD) analysis using Cu  $K_{\alpha}$  radiation (XRG 3100, Philips Electronic Instrument, Mahwah, NJ). The spectra obtained were compared to known spectra of similar perovskite compounds to determine phase concentration after background or noise removal using Jade+ v2.1 software (Materials Data Inc., Livermore, CA). The theoretical densities were calculated using the lattice parameters obtained from diffraction analysis. These theoretical densities can be compared to the bulk densities measured by the Archimedes method to determine if the samples are dense enough for oxygen permeation experiments. By comparing the bulk density to the theoretical density it is possible to determine the amount of open porosity in a sample.

### Archimedes Density

The Archimedes method was used for finding the apparent density of the sintered samples. The Archimedes Buoyancy Principle states that when an object is immersed in a liquid it will be lighter by an amount equal to the mass of the liquid that the object displaces. The density can then be calculated by collecting the dry, suspended, and wet weights of the sintered samples. The suspended and wet weights were obtained by submerging the samples in ethanol and then placing in a vacuum chamber until all the open pores of the sample had been infiltrated with the ethanol. The samples were then weighed as they were suspended completely immersed in a beaker of ethanol to obtain the suspended weight. By drying the sample and immediately weighing it, the wet weight was obtained before the ethanol could evaporate from the open pores, allowing a measurement of the bulk density of the samples to be calculated.

### Dilatometry

The coefficient of thermal expansion for the compositions shown in Table 1 was determined by dilatometric analysis (Unitherm Model 1161, Anter Laboratories, Inc., PA). Linear thermal expansion was conducted on bars (~1/6"x1/6"x1") at a ramp rate of 2°C/min in air. All dimensions were measured before the dilatometry. Data points were taken as the temperature increased and then decreased. As the temperature decreases, the slope of the line of the strain vs. temperature is calculated for thermal expansion coefficient values.

Electronic Conductivity

Electrical conductivity for the five compositions consisting of a single phase was measured using a four-point AC conductivity method. Platinum electrodes were attached as shown in figure 3.1.

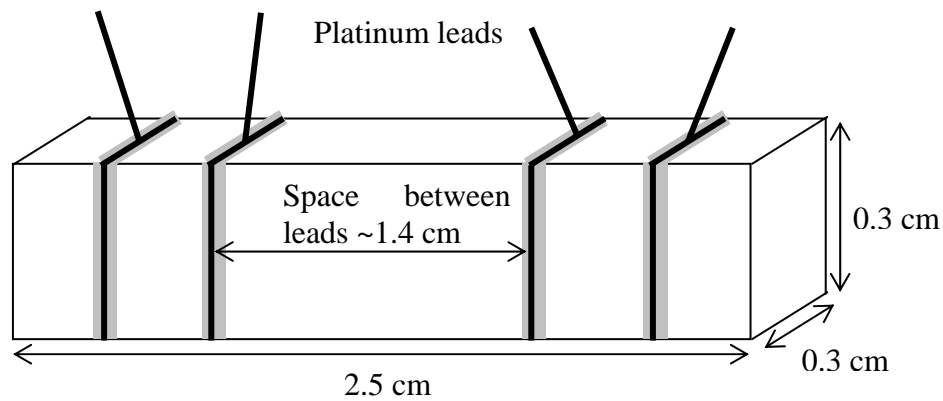


Figure 3.1: Sample used for the four-point AC conductivity experiments.

The samples were cut to the dimensions  $\sim 2.5$  cm x 0.3 cm x 0.3 cm and notched with a diamond saw where the platinum wraps were placed around the sample. Platinum paint was used to ensure the contact between the sample and the platinum electrodes. The paint was applied prior to the wires being wrapped and twisted on the samples and then cured at  $600^{\circ}\text{C}$ . The short leads that were wrapped around the samples were then welded to long leads for obtaining experimental data. The sample was then placed in a tube furnace with the leads connected to the current source and electrometer.

Ionic Conductivity

The amount of ionic conductivity was found by placing a 0.72-inch diameter sample in the setup shown in figure 3.2.

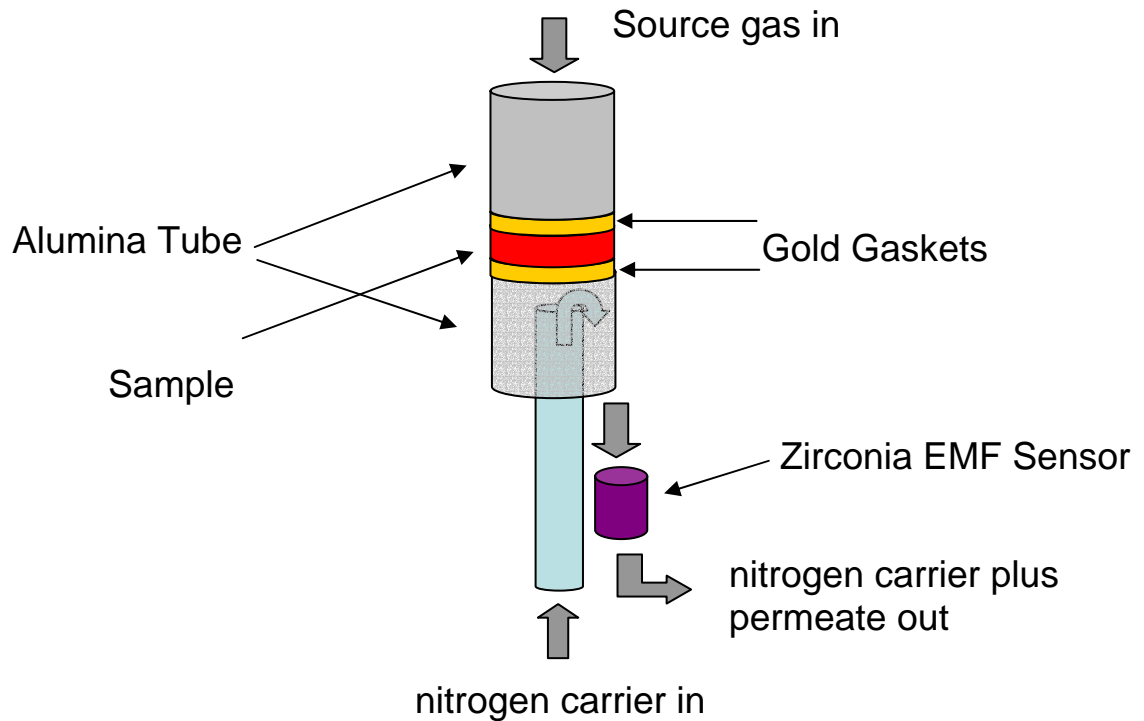


Figure 3.2: Oxygen permeation assembly.

After the thickness was measured, the sample was sandwiched between two alumina tubes with gold o-rings used to seal the sample to the tubes. The gold o-rings were super glued to the alumina tubes and the sample was glued to one of the tubes. Gravity and applied pressure provides an airtight seal from the alumina tube to gold and gold to sample interfaces. Therefore, the only gas that would cross from top to bottom would have to permeate through the sample. An outer alumina tube (not shown in figure

3.2) is used to provide stability to the structure and another interface seal to the gold. The furnace was ramped up to 950°C to allow the gold to liquefy sufficiently to form a seal but not ooze down the side. The furnace was then cycled from 950°C to 200°C at 2°C/min. Atmospheric air (20.98% oxygen) was flowed over the upper side of the sample at a rate of 100 cc/min. The lower side had nitrogen flowing at a rate of 25 cc/min. This created an oxygen gradient from one side of the sample to the other. The exhaust from the lower side was piped to a zirconia EMF oxygen sensor. The voltage measured from the sensor is a measure of the oxygen flux through the sample.

### Seebeck Measurements

In figure 3.3, a diagram of the assembly of the Seebeck coefficient measurement is shown.

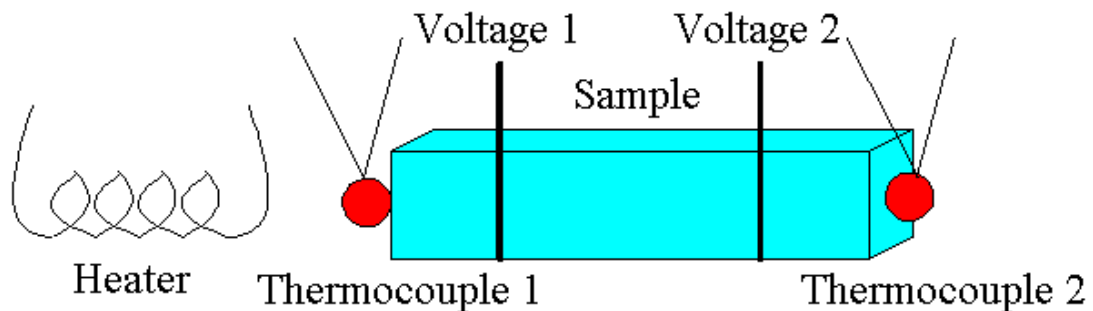


Figure 3.3: Assembly structure for Seebeck coefficient measurements.

On one end of a ceramic test bar, a heating element is used to create a temperature gradient across the sample with thermocouples on each end to measure the temperature gradient. Two voltage taps are placed on each end of the bar to measure the voltage drop

across the sample due to the applied temperature gradient. The entire sample is heated and cooled from 200°C to 900°C. At each 50°C interval measured on thermocouple 2, the temperature at thermocouple 1 was measured and used to calculate the temperature gradient between the two thermocouples. As the sample was heated from 200°C to 900°C, then cooled back to 200°C, the temperature difference ranged from -20°C to 30°C approximately fifteen data points are taken throughout this temperature gradient in order to allow an accurate line to be plotted through these points of voltage drop vs. the temperature gradient. The slope of the line of the voltage drop vs. the temperature gradient is the measured Seebeck coefficient.

#### Half – Cell Measurements

A diagram of the assembly of the half-cell measurement is shown in figure 3.4.

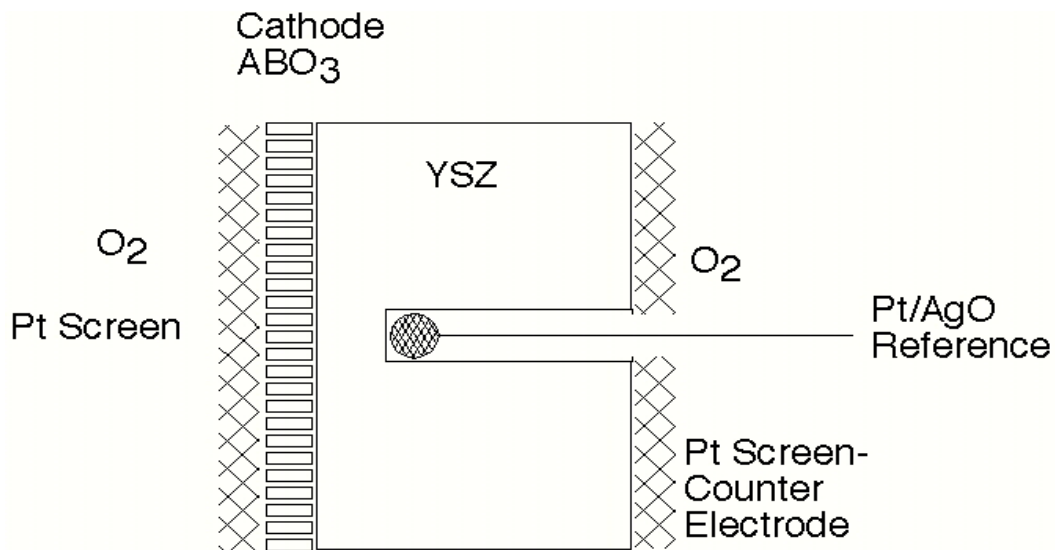


Figure 3.4: Half-cell measurement set-up.

Electrodes are screen-printed on yttria-stabilized zirconia (DKKK 8YSZ) pellets with 8 molar% yttria. These pellets have been uniaxially pressed at 6 MPa and then cold isostatic pressed at 500 MPa. The electrolyte pellet is 12.5 mm in diameter and 4 mm thick. A probe cavity is drilled to about 1 mm from the working electrode side.

After the electrolyte pellet is screen-printed with platinum on the side with the small hole and the opposite side has a cathode layer, the half-cell pellet is placed in between two platinum screens. A three-electrode cell configuration is used as illustrated in figure 3.4. A three electrode cell uses a working electrode, a counter electrode and a reference electrode to make the half cell measurement. A Lugin-Haber type reference electrode was used in the assembly [30]. A 0.5 mm platinum wire with a 0.75 mm silver bead on the tip is pressed into the hole in the sample. This wire is used as a reference point to minimize the resistance through the electrolyte. Alumina plungers are affixed to an alumina tube using spring tension and are used to provide good contacts for the platinum screens and cathode and platinum layers on the half-cell pellet. The working electrode is the cathode side while the counter electrode is the platinum side of the half-cell. By connecting this assembly to a Solartron SI 1287 potentiostat/galvanostat, half-cell potential is measured through the use of cyclic voltamograms with current interrupt embedded in the software program. The applied current ranged from  $-2\text{A}$  to  $2\text{A}$  with the voltage drop ranging from  $-0.5\text{V}$  to  $0.5\text{V}$ , which limited the current range with a scan rate of  $10\text{mV/sec}$ . This current vs. voltage curve can be modeled using a hyperbolic sine curve to determine the resistance in the cathode and the current exchange density of the cathode-electrolyte interface.

## CHAPTER 4

## RESULTS AND DISCUSSION

XRD EvaluationPhase Purity Peaks

Figure 4.1 shows XRD phase peaks for the entire PSM data set after calcination at 1400°C for an hour. A silicon powder was used as a reference to allow aligning the phase peaks if there is offset among the data. The XRD peaks in figure 4.1 from the top progress through the sample from PSM 10, 20, to 30 and then the A site deficient ceramics with PSM 20 A to PSM 30 A.

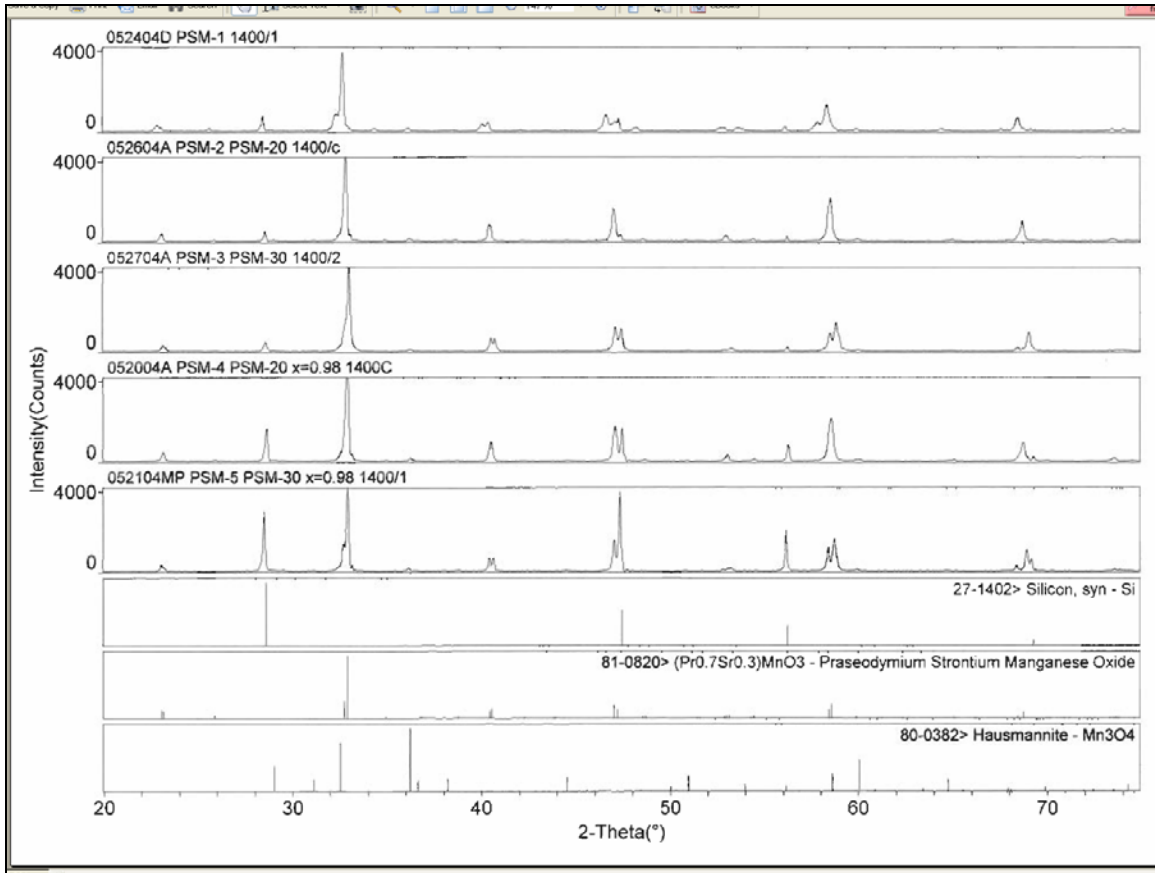


Figure 4.1: XRD phase peaks for the PSM data set with references for silicon, PSM and Hausmannite.

The different phase peaks of the sample set show that each sample develops into a single perovskite phase, however a slight peak showing a slight excess in manganese is detectable, which develops a hausmannite phase,  $Mn_3O_4$ . XRD peaks show phases in ceramic with at least a five percent phase concentration throughout the structure; and thus throughout these ceramics, five percent of their structure contains this hausmannite phase. As the strontium concentration increases, the excess of manganese is more prevalent with slightly stronger peaks. The A site deficient ceramics contained slightly

stronger peaks overall than its stoichiometric partner, and even PSM 20 A has more manganese in the hausmannite phase than PSM 30. This phase may disappear with an increased sintering temperature or a longer sintering time or both.

### Relative Density

From the lattice parameters that are calculated from the shifts and width of the phase peaks from X-ray diffraction, the theoretical density, which is a calculation of the density of the ceramic material without porosity, can be calculated. Through the Archimedes density approach discussed earlier, the actual density of a ceramic bar can be calculated and then compared with the theoretical density to determine the percent density. In table 3, calculations of the bulk density and percent density, which is the bulk density/theoretical density, of the sample set can be found.

Table 3: Relative and percent densities calculations

Ceramic	Dry Mass (g)	Suspended Mass (g)	Saturated Mass (g)	Theoretical Density	Bulk Density	Percent Density
PSM 10	9.793	8.561	9.808	6.5594	6.17	94.1
PSM 20	8.952	7.824	8.956	6.5844	6.21	94.4
PSM 20 A	7.559	6.593	7.573	6.6021	6.06	91.8
PSM 30	7.614	6.64	7.624	6.6207	6.08	91.8
PSM 30 A	14.542	12.688	14.544	6.6865	6.12	91.6

The equation used to find the bulk density of the material is as follows:

$$\rho_{\text{bulk}} = \frac{\rho_{\text{ethanol}} \cdot m_{\text{dry}}}{m_{\text{sat}} - m_{\text{sups}}}$$

where  $m_{\text{dry}}$ ,  $m_{\text{sat}}$ , and  $m_{\text{sups}}$  are the dry mass, saturated mass and suspended mass respectively.

These relative densities need to be about 95% dense and therefore each sample was sintered at 1500°C for 2 hours at a ramp rate of 2°C/min. After this sintering, the ceramic bars and pellets would be dense enough to properly measure the oxygen permeation, electrical conductivity, and Seebeck coefficient.

### Dilatometry

#### Sintering Study

After calcination at 1200°C for 2 hours a sintering study was performed to determine the temperature at which the ceramic densifies and the temperature to which an ink preparation would expect to adhere to an electrolyte pellet for half-cell testing. This data is shown in figure 4.2.

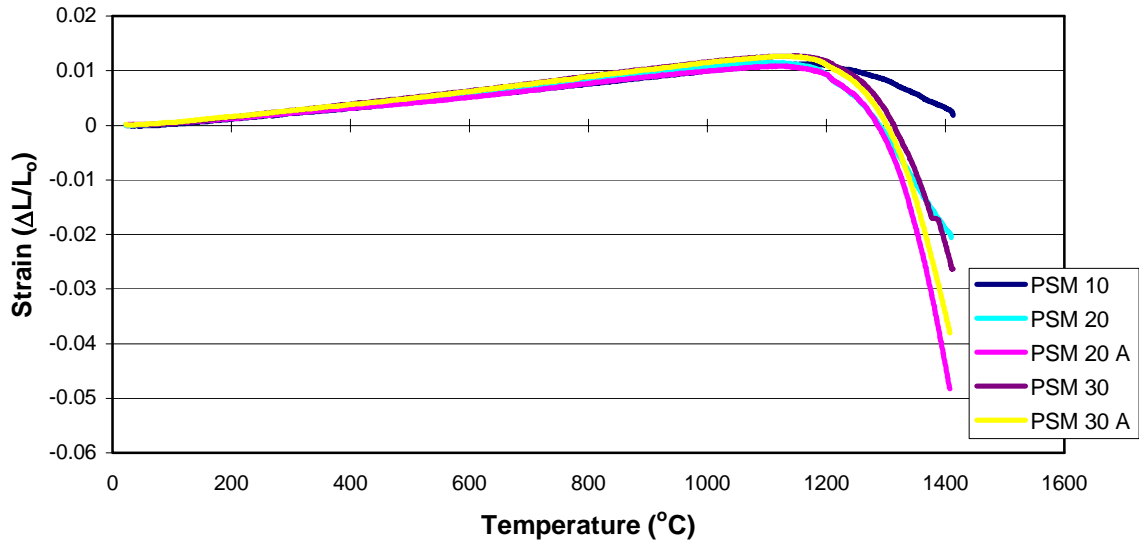


Figure 4.2: Densification Study of samples up to 1400°C.

### TEC Calculation

The thermal expansion coefficient was determined using the data from the dilatometer. After the sintering study, data of strain vs. temperature as the temperature decreased was taken. The slope of this line through the temperature range of 200°C to 1400°C was calculated for the thermal expansion coefficient and is shown in figure 4.3. The thermal expansion coefficients for a common electrolyte (8YSZ) and anodic material (NiO-YSZ) are also displayed on this graph in order to compare the sample set with commonly used solid oxide fuel cell material.

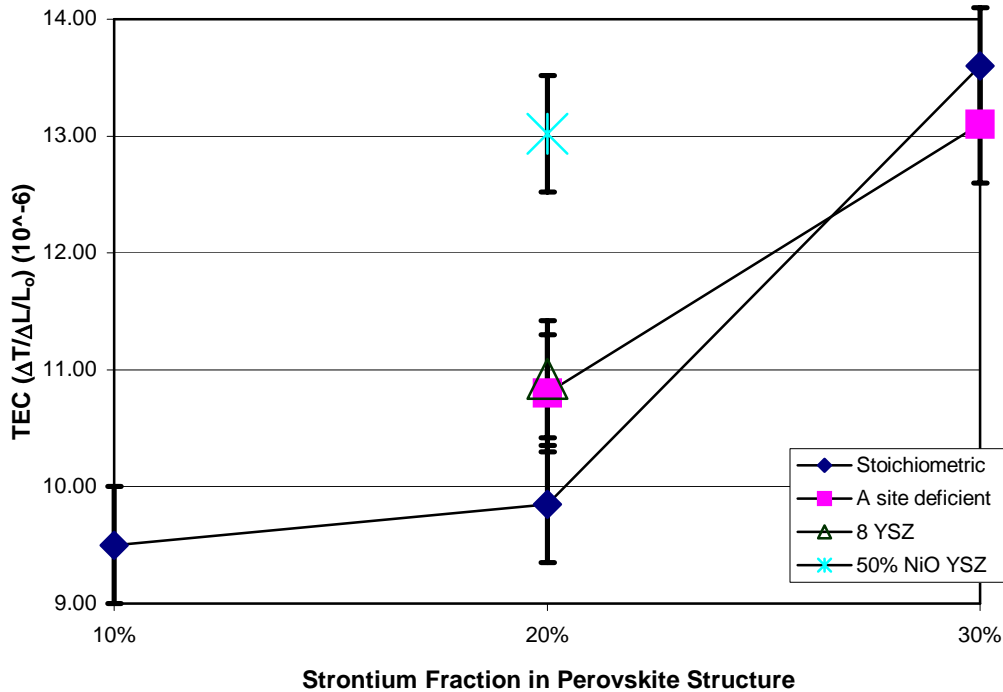


Figure 4.3: TEC measurements of sample set with comparison to common electrolyte and anode material.

### Analysis

In the sintering study, the graph in figure 4.2 should eventually level off to display the maximum density observed by the ceramic material; however, due to limitations of the experimental setup, a full range of temperatures was not able to be completed. A more useful calculation from this data is an expected sintering temperature for adhesion to the YSZ electrolyte material. This will occur near the “knee” of the graph or at the point where the ceramic starts to densify. The temperature that was tested successfully for this adhesion was 1150°C. Also apparent in the sintering curve is the trend in

densification as the strontium concentration is increased. As strontium concentration increased so did the temperature at which full densification occurred. By creating an A site deficiency in the matrix, the densification temperature is also increased. PSM has very refractory material properties, which contributes to high sintering temperature throughout the sample set.

The strain vs. temperature line that was used to determine the thermal expansion coefficient (TEC) was linear throughout the temperature range, which means that the sample's structure was very stable. As the strontium concentration increases, the TEC value also increases. The A site deficient set follows the same trend and is within the margin of error of the corresponding stoichiometry set. These coefficients are also compared with commonly used solid oxide fuel cell materials in figure 4.3. 8YSZ is right in the middle of the sample set with PSM 20 having the same coefficient. The anode material Ni-YSZ is at the high end of the TEC coefficient but at the same level as PSM 30. Therefore, the ceramic materials tested in the sample set can all be used with Ni-YSZ except PSM 10 because the coefficients differ by more than  $3 \times 10^{-6}$  [1].

### Electronic Conductivity

#### Calculations

Electrical conductivity data are shown in the figure 4.4 for the complete data set for the temperature range from 200°C to 950°C using a four point AC testing method as discussed earlier.

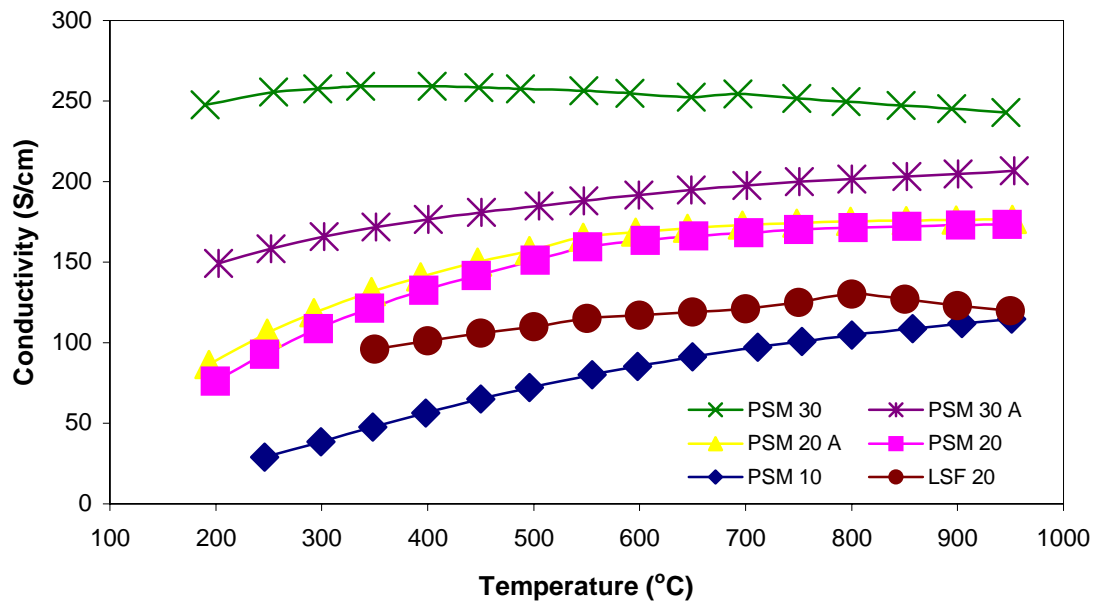


Figure 4.4: Electrical conductivity measurement from 200°C to 950°C.

The conductivity values presented in figure 4.4 are for the bulk electrical conductivities of the samples. Since the ionic conductivity is less than 1% of this bulk conductivity, the values are regarded as dominantly electronic. The single phase compositions tested (except for PSM 30) exhibited an increase in electrical conductivity with increasing temperature. This behavior is typical for small polaron conductors where the electronic conductivity of the material is dependant on the mobility of thermally activated localized charges.

All of the compositions had a temperature where their conductivity leveled off and then decreased or stayed constant. For example, the electrical conductivity for PSM 20 increased with increasing temperature until it reached about 600°C, where it leveled off or increased only slightly. This is most likely due to a saturated state of electrons in the conducting band.

An Arrhenius plot is constructed in figure 4.5 where the natural log of the electrical conductivity multiplied by the temperature is graphed versus the inverse temperature. The activation energies can be determined from the slopes of these curves and are plotted in figure 4.6 for comparison.

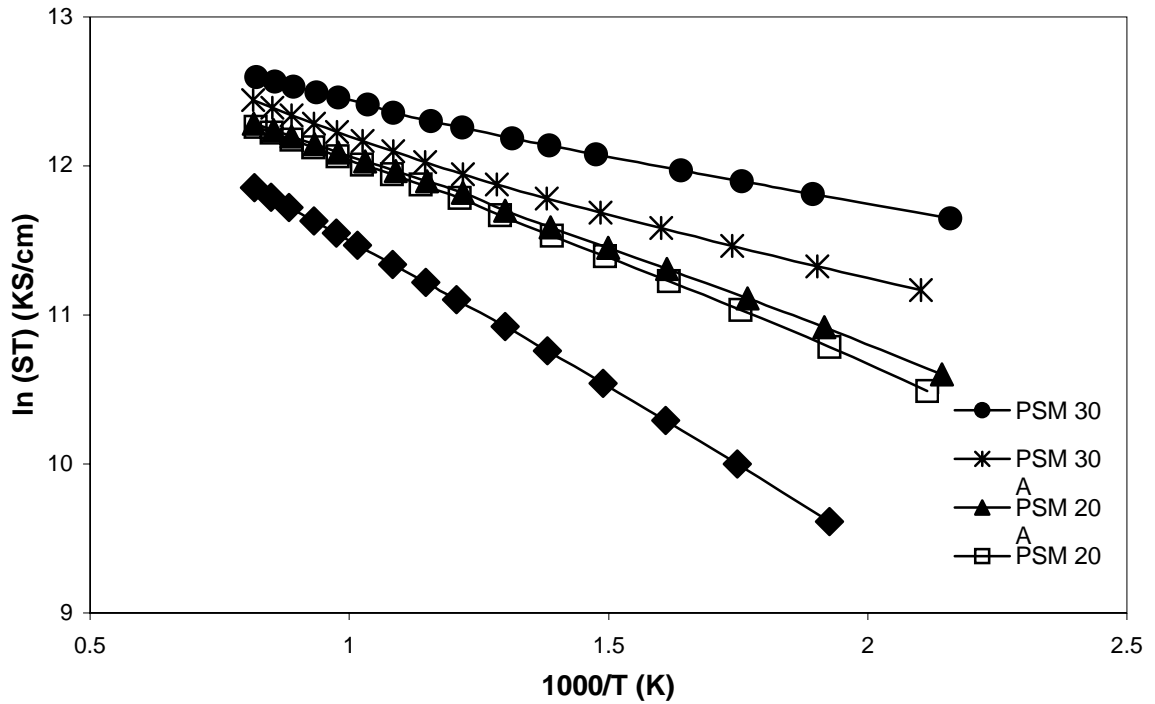


Figure 4.5: Arrhenius plot of electrical conductivity measurement.

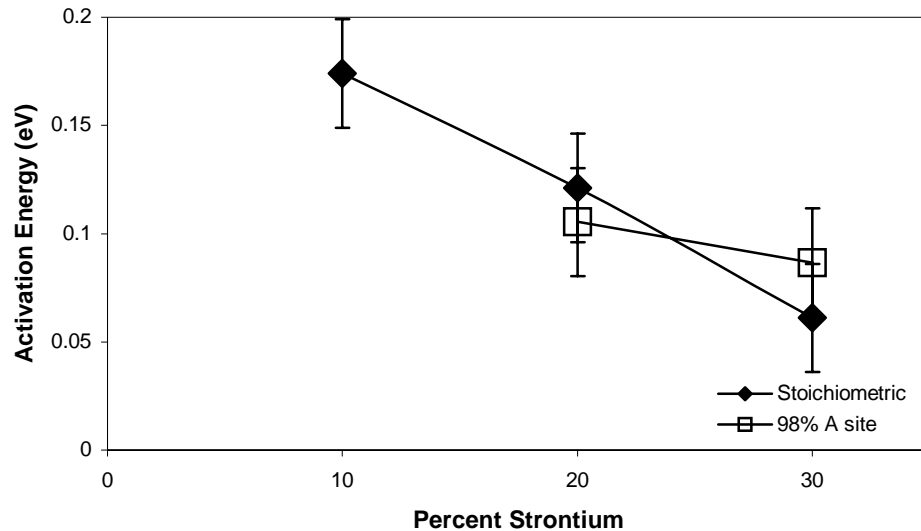


Figure 4.6: Activation energies for electrical conductivity.

### Analysis

The electrical conductivity is an important factor in determining the effectiveness of a cathode material. Typically a conductivity value of 100 S/cm in the temperature range of 600°C to 800°C is preferable [8]. The sample set, except for PSM 10, all reached this value and in fact doubled and almost tripled this value. PSM 10 barely reached 100 S/cm at 800°C. As the strontium concentration increased, the activation energy to create conductance decreased. The activation energy is the necessary energy to raise electrons to the conduction band. Therefore, the activation energy is an inverse function of the total conductance throughout this sample set. Lower activation energy of electrical conductivity translates to a raise in the ease of conductance and therefore a higher conductivity level can ensue.

A comparison of the PSM sample set with a commonly used cathodic material set, lanthanum strontium ferrite (LSF) is shown in figure 4.4. The PSM sample set, except

for PSM 10, has a significantly higher electrical conductivity than that of LSF 20, which should translate into a higher cathode effectiveness in the solid oxide fuel cell.

### Ionic Conductivity

#### Calculations

The ionic conductivity was determined by measuring the flux of oxygen that permeated through a sample of known dimensions. The following equation was used to determine the ionic conductivity [1].

$$\sigma = \frac{4FJt}{RT \ln \left[ \frac{Po_2^1}{Po_2^2} \right]}$$

where F is Faraday's constant, J is the oxygen flux, t is the sample thickness, K is the Boltzman constant, T is the absolute temperature,  $Po_2^1$  and  $Po_2^2$  are the oxygen partial pressures above and below the sample. The use of this equation requires the assumption that the oxygen flux is dominated by the bulk ionic conductivity and not the surface kinetics. In figure 4.7 oxygen permeation data is shown for the sample set for temperatures of 200°C to 950°C.

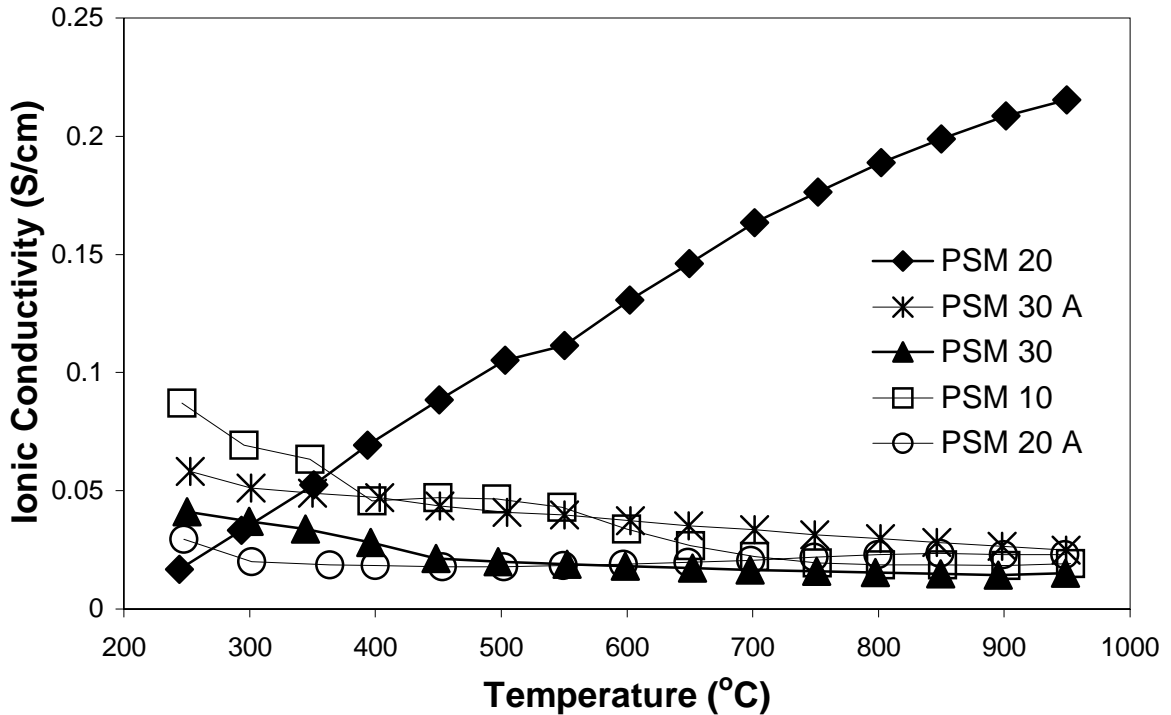


Figure 4.7: Oxygen permeation from 200°C to 950°C.

### Analysis

The oxygen permeation for PSM 20 behaved as initially expected through research of similar ceramics. In this sample, the oxygen flux through the sample increases as the temperature increases. This correlates to a thermally activated response to ionic conductivity. Each sample was tested through the temperature regime at least three times to improve data accuracy, and each data set, including PSM 20, had the same conductivity through this temperature range for each temperature sweep. The oxygen permeation data for the rest of the series shows little to no ionic conductivity through the temperature range of 600°C to 950°C. At lower temperatures, the oxygen permeation

slightly increases as the temperature decreases. The major conclusion to draw from this data is that the ionic conductivity for much of the series is negligible through the temperature range of a typical operating solid oxide fuel cell except for PSM 20.

### Seebeck Measurements

#### Calculations

The Seebeck coefficient is displayed through the temperature range of 100°C to 950°C in figure 4.8. This coefficient is a measurement of a voltage drop created as a result of a temperature gradient across a ceramic bar.

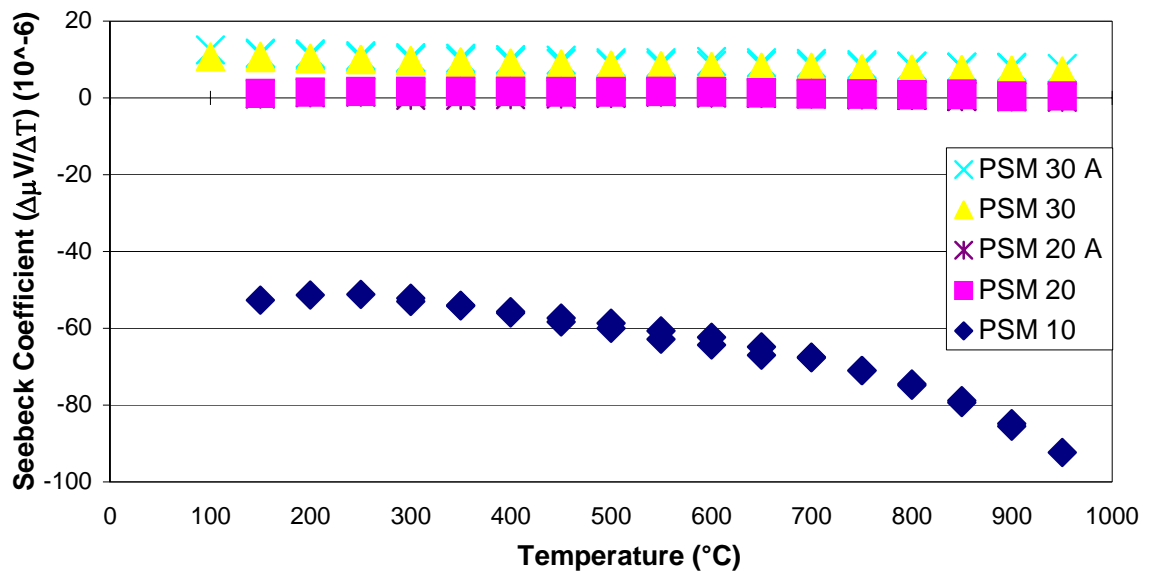


Figure 4.8: Seebeck measurements for the sample set from 100°C to 950°C.

### Analysis

The law of Magnus states that for a material that is homogenous and isotropic, the Seebeck EMF is independent of the temperature distribution within the material and depends only on the temperature at the junctions. The Seebeck EMF satisfies the following equation [33]:

$$V_{ab}(T_1, T_2) = V_{ab}(T_1, T_c) + V_{ab}(T_c, T_2)$$

where  $T_1$ ,  $T_2$ , and  $T_c$  are arbitrary temperatures.

The Seebeck coefficient is defined by the following equation [33]:

$$\alpha_{ab}(T_1) = \lim_{T_2 \rightarrow T_1} \frac{V_{ab}(T_1, T_2)}{T_2 - T_1}$$

where  $\alpha_{ab}$  is the Seebeck coefficient. Note that the Seebeck coefficient is not dependent on some arbitrary  $T_c$  temperature but only  $T_1$  and  $T_2$ . To apply this equation, one side of the bar had a fixed temperature and the opposite side's temperature was varied to create the temperature gradient. The slope of the line of voltage drop versus temperature gradient is calculated when the temperature gradient passes through zero.

The Seebeck coefficient should increase in magnitude with an increased temperature if the electrical conductivity increases with temperature and a simple mechanism of conductance exists within the structure of the ceramic. PSM 10 shows this dependence on temperature. For a true small polaron conductor, an increase in Seebeck coefficient is expected as the strontium concentration increases within the matrix because the electrical conductivity and the charge carrier concentration increase. The Seebeck

coefficient should increase as well. However, this behavior did not always occur. Between PSM 10 and 20, the electron conduction became more complicated. In PSM 10, the electrons mainly traveled from the high temperature side to the cooler temperature, while the rest of the PSM series performed the opposite dominant traveling. An n-type conductor has a negative Seebeck coefficient and a p-type conductor has a positive Seebeck coefficient. Therefore between PSM 10 and 20, the ceramic structure changed conductor types from n to p. Considering the ionic conductivity of the series was negligible, except for PSM 20, a true electrical conductance can be observed. PSM 20 exhibited a balance between n and p type conduction and as the strontium concentration increased the Seebeck coefficient increased as well.

### Half – Cell Measurements

#### Calculations

Half cell measurements are shown with current versus the cathode potential in figure 4.9. These measurements were performed using a Solartron SI 1287 potentiostat/galvanostat. Cyclic voltamograms using a current interrupt technique were utilized for this measurement.

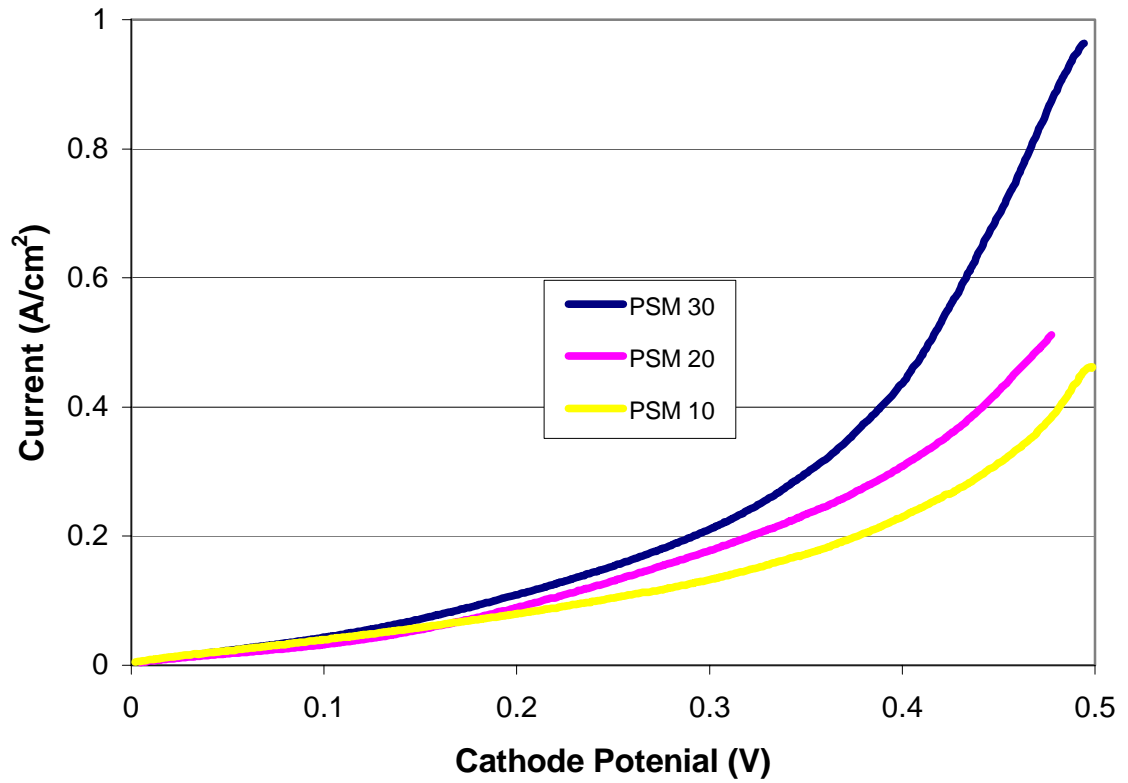


Figure 4.9: Half cell measurement for sample set at 850°C in air.

PSM 10 data at 850°C with air and pure oxygen on the cathode side are shown with a hyperbolic sine curve in order to model the area specific resistance and the overall chemical reaction constant in figure 4.10.

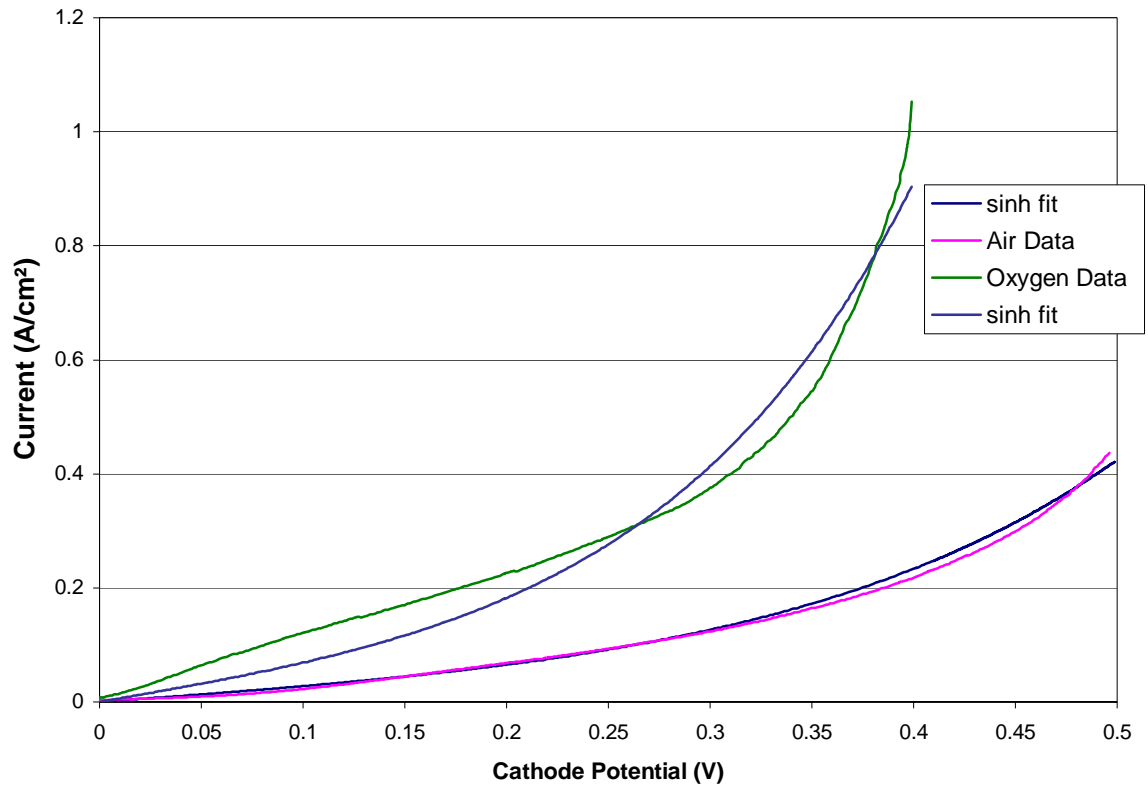


Figure 4.10: Example of hyperbolic sine curve fit to PSM 10 data at 850°C.

In the table below, the entire PSM series from 700°C to 850°C was modeled with a hyperbolic sine curve in order to compute electrocatalytic activity.

Table 4: Tabulated values of chemical reaction constants and area specific resistance throughout the cathode layer.

Ceramic		850°C		800°C		750°C		700°C	
		Oxygen	Air	Oxygen	Air	Oxygen	Air	Oxygen	Air
PSM 10	I <sub>o</sub>	0.02205	0.0398	0.0252	0.0022	0.0026	0.00074	0.00022	0.00007
	R <sub>ASR</sub>	1.6036	3.8294	3.4823	23.645	24.246	85.899	275.39	889.57
PSM 20	I <sub>o</sub>	0.055	0.0227	0.0404	0.0045	0.0029	0.00107	0.00045	0.00031
	R <sub>ASR</sub>	1.4536	3.468	2.4613	14.269	22.29	58.956	141.227	204.65
PSM 20 A	I <sub>o</sub>	0.0859	0.0299	0.0141	0.0032	0.00183	0.00103	0.00046	0.00034
	R <sub>ASR</sub>	1.326	3.152	5.4933	20.231	32.642	61.339	135.81	185.26
PSM 30	I <sub>o</sub>	0.0526	0.0142	0.0221	0.0066	0.0043	0.0023	0.00107	0.0008
	R <sub>ASR</sub>	1.409	4.179	3.341	9.887	15.022	27.966	59.289	79.566
PSM 30 A	I <sub>o</sub>	0.0874	0.0327	0.0407	0.0067	0.0036	0.00148	0.00078	0.00053
	R <sub>ASR</sub>	1.256	3.074	5.685	11.422	18.119	42.907	80.61	119.95

\*Note: I<sub>o</sub> is in A/cm<sup>2</sup> and R<sub>ASR</sub> is in Ω/cm<sup>2</sup>

The entire series of cathodes pictured in figures 4.11 to 4.15 were sintered on individual YSZ electrolytes at 1150°C for 2 hours. The scanning electron microscope picture of the half cell of PSM 10 after the cathodic overpotential was measured is shown in figure 4.11. The porous cathode layer pictured in figure 4.11 is about 3 μm thick and is well adhered to the dense YSZ electrolyte. Energy Dispersive Spectrometer (EDS) measurements were used to identify the molar percentage of different elements in the cathode structure. The darker regions contained more manganese while the lighter regions contained more praseodymium. By scanning the entire region, the molar concentration of praseodymium was approximately 90 % of the molar concentration of manganese and the molar concentration of strontium was approximately 10 % of the molar concentration of manganese. Also, scanning the YSZ electrolyte, migration of praseodymium, strontium, or manganese was not discovered. This suggests that there were no adverse reactions with the cathode layer of PSM and the YSZ electrolyte. This

would eliminate the barrier layer between the cathode layer and the electrolyte that is currently being employed. This is very beneficial because it eliminates one processing step and therefore reduces production cost of the fuel cell plate.

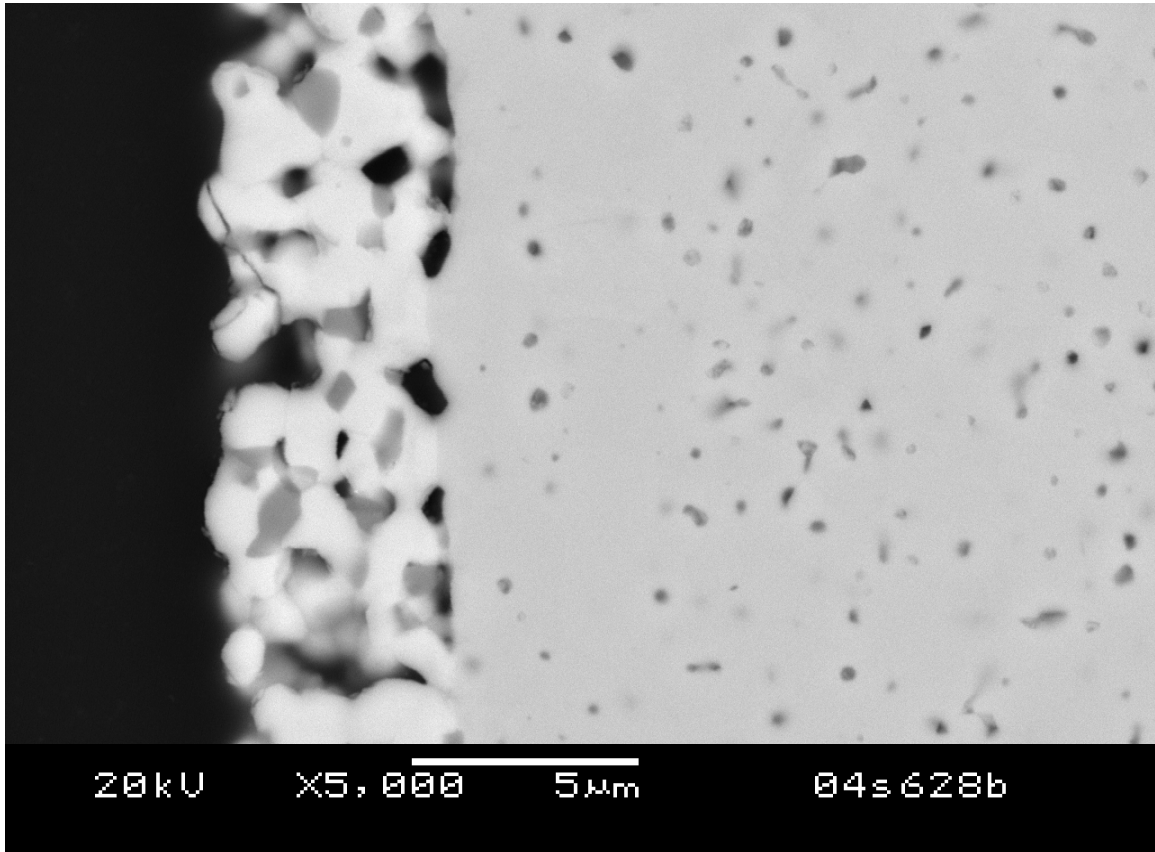


Figure 4.11: PSM 10 half cell after testing.

The scanning electron microscope picture of the half cell of PSM 20 after the cathodic overpotential was measured is shown in figure 4.12.

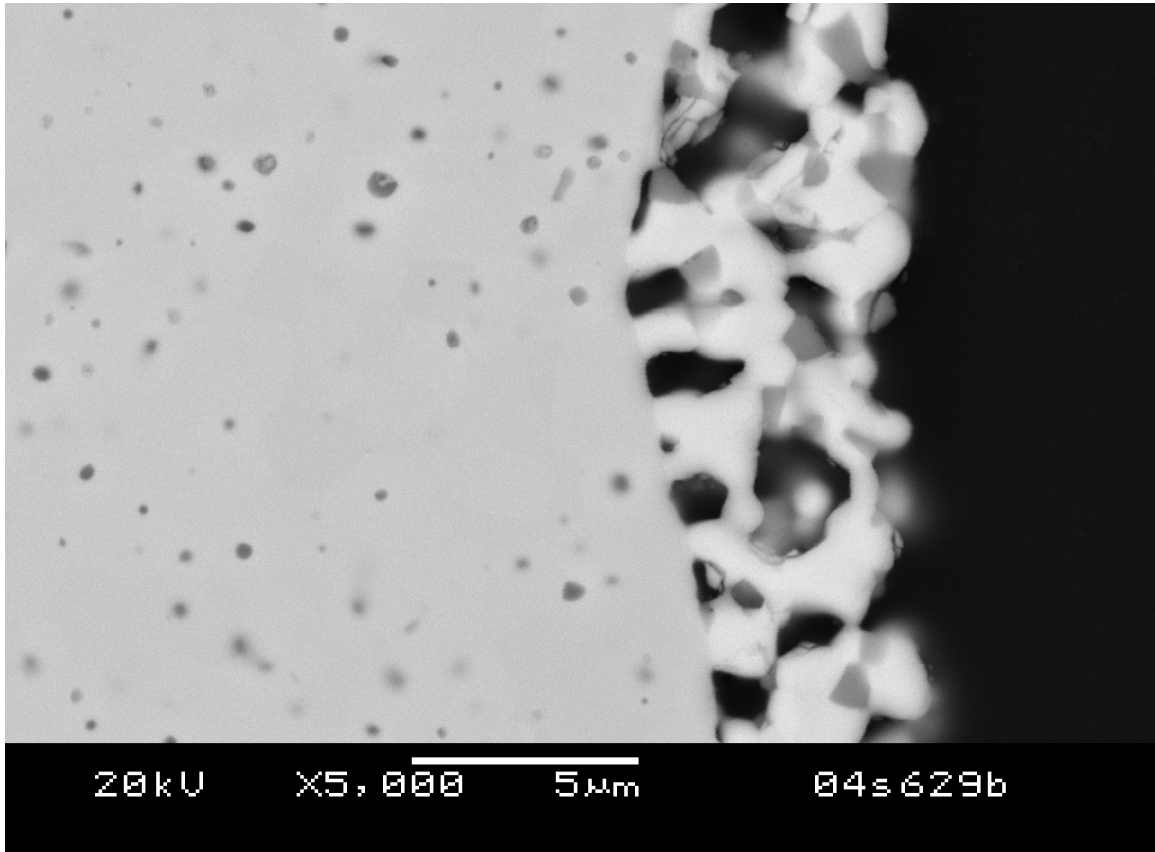


Figure 4.12: PSM 20 half cell after testing.

The scanning electron microscope picture of the half cell of PSM 20 A after the cathodic overpotential was measured is shown in figure 4.13.

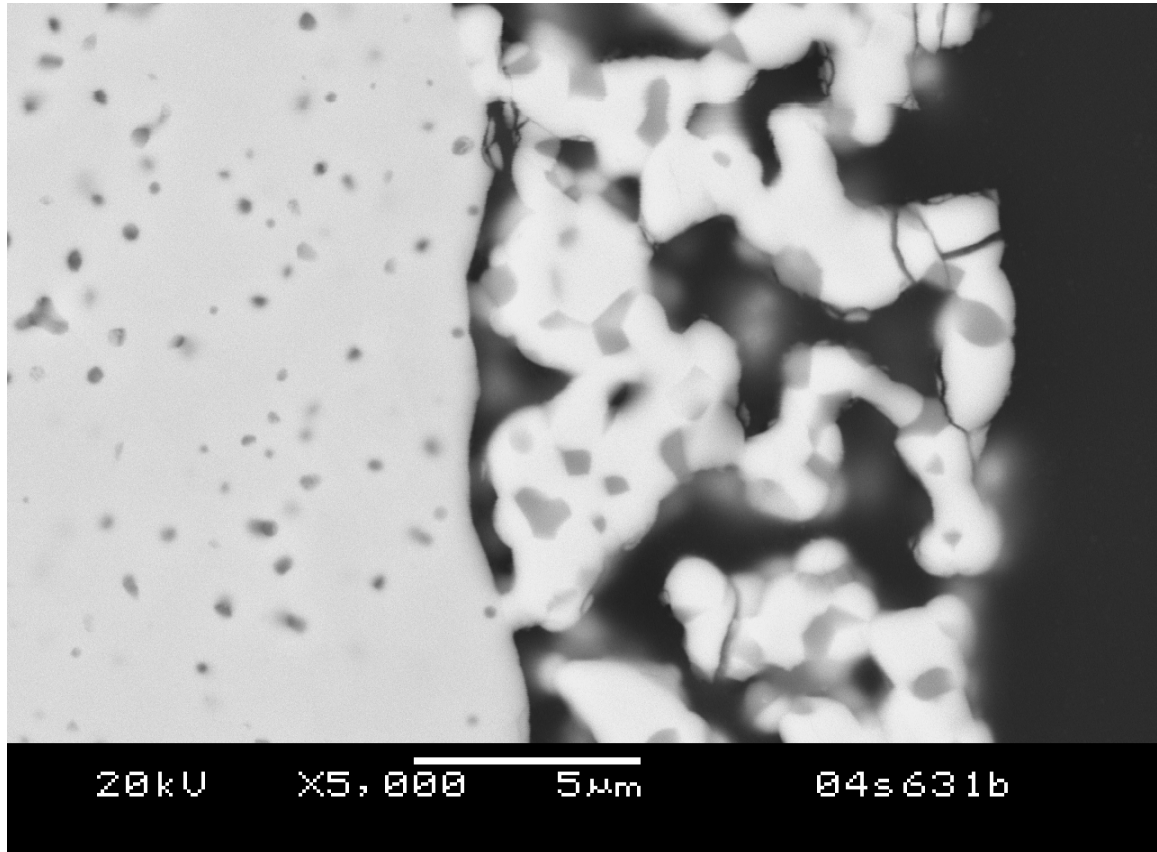


Figure 4.13: PSM 20A half cell after testing.

The scanning electron microscope picture of the half cell of PSM 30 after the cathodic overpotential was measured is shown in figure 4.14.

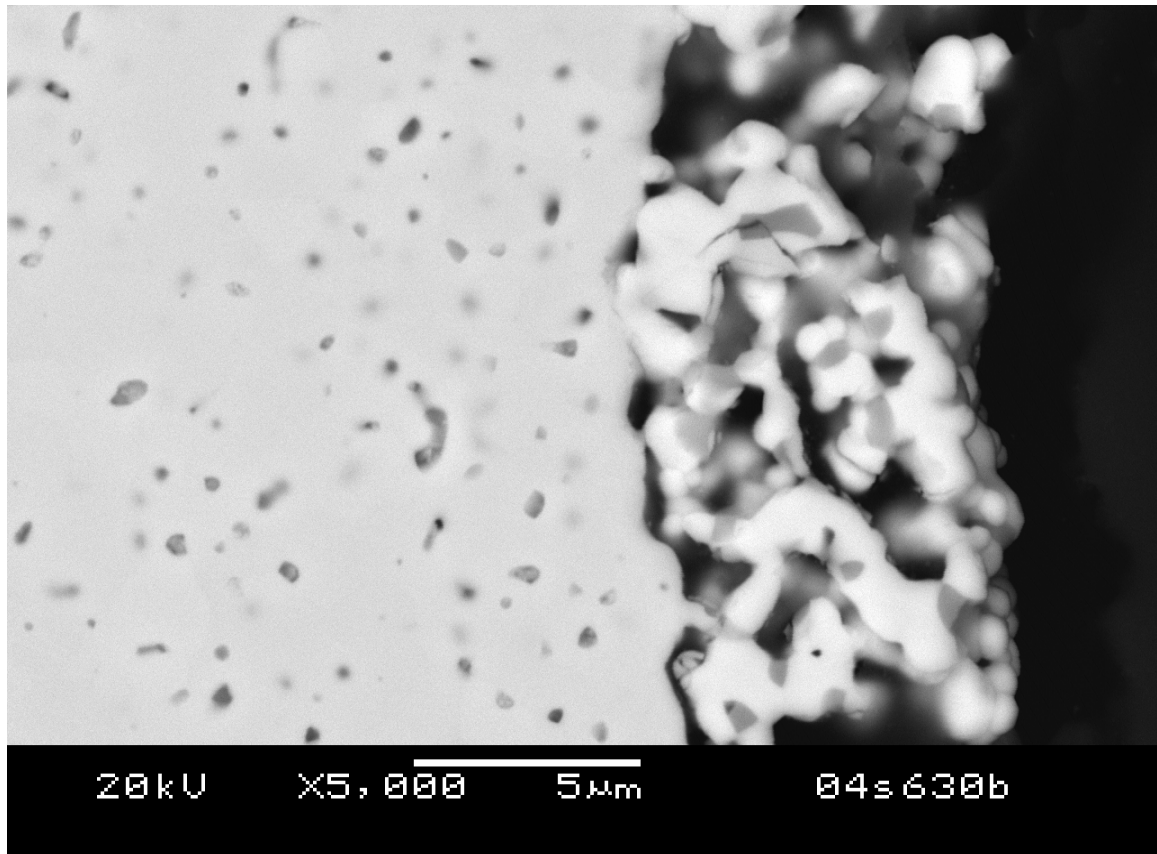


Figure 4.14: PSM 30 half cell after testing.

The scanning electron microscope (SEM) picture of the half cell of PSM 30 A after the cathodic overpotential was measured is shown in figure 4.15.

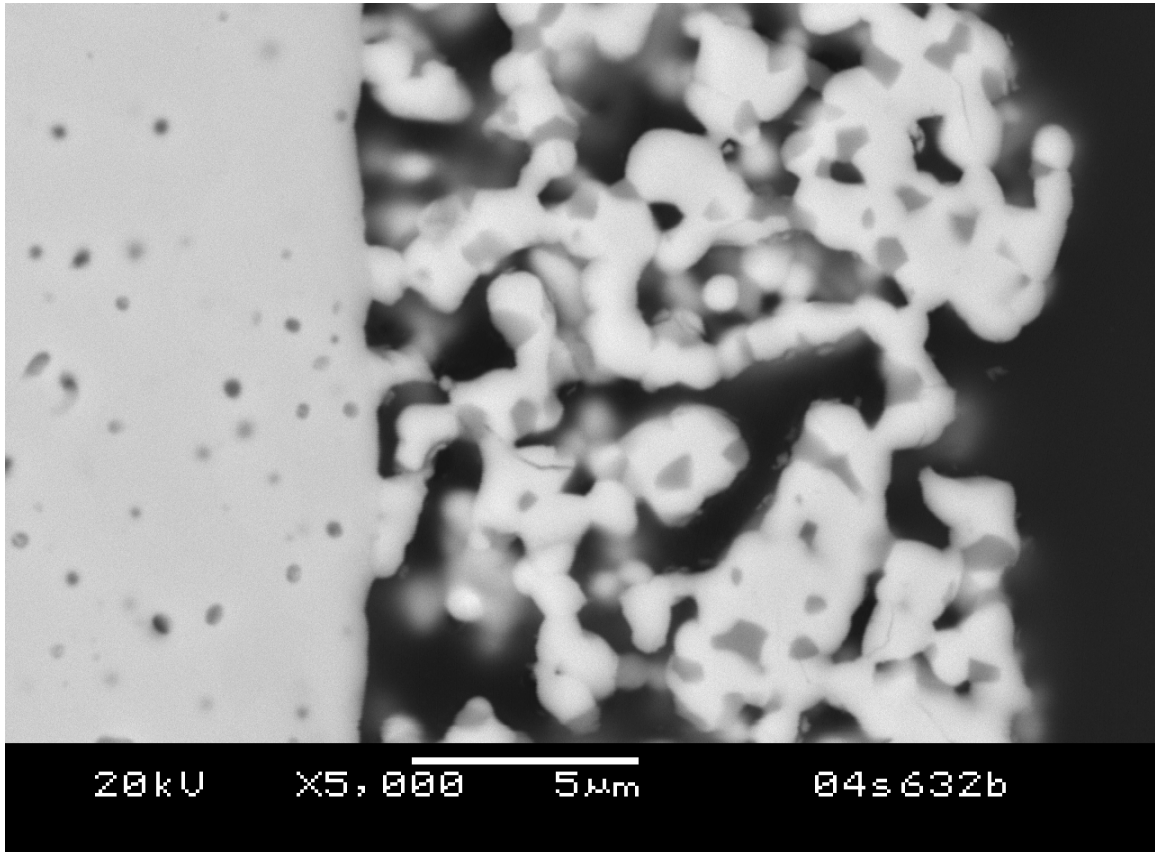


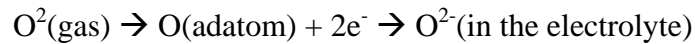
Figure 4.15: PSM 30A half cell after testing.

Some trends can be interpreted from the series of SEM pictures. As the strontium concentration increases, the porosity of the cathode layer also increases and the A site deficiencies have more porosity than their stoichiometric partner with PSM 20 A having higher porosity than even PSM 30. As this porosity increases, the thickness of the cathode layer also increases. PSM 30 A's cathode layer thickness is about 12  $\mu\text{m}$  while PSM 10's is about 3  $\mu\text{m}$ . Each ceramic in this series adhered well to the YSZ electrolyte

after sintering at 1150°C for 2 hours. Considering the oxygen permeation is negligible for the PSM series except PSM 20, porosity in the cathode layer is a very important parameter in order to have enough oxygen flux to the triple phase boundary to increase the reduction reaction. This parameter and the electrical conductivity of the series correlates well with the cathodic overpotential measurements, meaning as the porosity and electrical conductivity increase, the cathodic overpotential is lower.

### Analysis

These half cell measurements show the electrocatalytic activity of the cathode itself. The chemical reaction on this side is as follows:



A hyperbolic sine curve is used to model these curves to better interpret the graphs. Through the use of this equation, the chemical reaction constant of the equation above and the area specific resistance can be computed. This equation is as follows:

$$I = I_0 \cdot \left( e^{\frac{\alpha_a \cdot F}{R \cdot T}} + e^{\frac{\alpha_c \cdot F}{R \cdot T}} \right) = 2 \cdot I_0 \cdot \sinh\left(\frac{\alpha \cdot F \cdot \eta}{R \cdot T}\right)$$

where  $I$  is the current,  $F$  is the Faraday's constant,  $R$  is the ideal gas constant,  $T$  is the temperature,  $\eta$  is the voltage.

$$\frac{1}{R_{\text{ASR}}} = \frac{I}{\eta} = 2I_0 \cdot \left(\frac{\alpha \cdot F}{R \cdot T}\right)$$

where  $R_{\text{ASR}}$  is the area specific resistance.

By looking at Table 4, trends in the PSM series can be observed. As the strontium concentration increases, the area specific resistance decreases and the chemical reaction constant increases. For the entire series, temperature dependence is observed; as temperature decreases, the electrocatalytic performance of the cathode significantly decreases, especially at 700°C.

## CHAPTER 5

## CONCLUSIONS AND RECOMMENDATIONS

The PSM series was characterized through the use of a variety of experimental methods. XRD was used to interpret the phases in the series to determine if a single phase perovskite structure could be made after calcination of the ceramic at 1400°C for two hours. A sintering study was additionally performed to determine the temperature of full densification and an effective sintering temperature to adhere to the YSZ electrolyte. Densification happens at 1500°C, while the cathode ink was sintered on the electrolyte at 1150°C.

The electrical conductivity also was measured using a standard four probe AC measurement technique. These conductivity measurements showed a higher conductivity than the traditional LSM cathode material. An upper limit on the conductivity seemed to be above 30% strontium concentration; therefore, more research should be performed with strontium concentrations above 30% until this upper limit can be determined. The activation energies for these conductivities were also calculated using an Arrhenius plot, with these activation energies decreasing as the strontium concentration increased.

The oxygen permeation of this series was measured using an oxygen transport method. Except for PSM 20, the oxygen conductivity was negligible for the series. More research should be undertaken in order to increase the oxygen flux through the sample and to determine the mechanism of transport through PSM 20. SEM pictures of the used

pellets can be used to determine densification and find any cracks in the pellets. The addition of another multivalent dopant on the B site may increase the oxygen permeation.

Another measurement was the Seebeck coefficient, which determined that the electrical conduction of the ceramic changed from an n type conductor to a p type conductor as the strontium concentration increased. More research should be performed to better understand this phenomenon with PSM 5 and PSM 15 being a good start to this further research. Thermogravimetric analysis should be used to determine the charge carrier concentrations for the data set.

The cathodic overpotential was measured through the use of cyclic voltamograms using a current interrupt technique. The cathodic overpotential lowered as the strontium concentration increased. This correlates well with the electrical conductivity measurements. Calcination at 1200°C does not produce a single phase structure for these materials. Therefore, the ceramic powders should be calcined at 1400°C instead; and then more inks should be prepared and tested. These results could be compared with the results from this study to determine the importance of having a single phase perovskite structure.

## SOURCES CITED

- 1 N. Q. Minh, *Science and Technology of Fuel Cells*, eds F. Seitz and P. Tunbull, Vol 3 (Elsevier Science, Amsterdam, 1995).
- 2 N. Q. Minh, *Journal of America Ceramic Society*, **76** 563 (1993).
- 3 Y. Teraoka, T. Nobunaga, K. Okamoto, N. Miura, N. Yamazoe, *Solid State Ionics*, **48** 207-212 (1991).
- 4 Solid State Energy Conversion Alliance (SECA) <http://www.seca.doe.gov/>. April 10, 2004.
- 5 S. Gopalan, *Cathode Materials for Intermediate Operating Temperature SOFC*, May 30, 2003.
- 6 T. Tsai, S.A. Barnett, *Journal of Electrochemical Society* **142** 3084 (1995).
- 7 T. Ishihara, T. Kudo, H. Matsuda, Y. Takita, *Journal of Electrochemical Society*, **142** 1519 (1995).
- 8 I. Reiss, *Solid State Electrochemical Cells*, Physics Dept., Techion-IIT 2000.
- 9 H. Kruidhof, H. J. M. Bouwmeester, R. H. E. v. Doorn, A. J. Burggraaf, *Solid State Ionics* **63-65**, 816-822 (1993).
- 10 J. W. Stevenson, T. R. Armstrong, R. D. Carneim, L. R. Pederson, W. J. Weber, *Journal of the Electrochemical Society* **143**, 2722-2729 (1996).
- 11 T. Sasaki, Y. Matsutmoto, J. Hombo, M. Nagata, *Journal of Solid State Chemistry*, **105** 255 (1993).
- 12 S. P. Simner et al., *Solid Oxide Fuel Cells VII, Electrochemical Soc. Proc.*, Electrochemical Society, Philadelphia, PA 2001.
- 13 J. Will, A. Mitterdorfer, C. Kleinlogel, D. Perednis, L.J. Gauckler, *Solid State Ionics* **131** 79-96 (2000).
- 14 M. Mogensen, N.M. Sammes, G.A. Tompsett, *Solid State Ionics* **129** 63-94 (2000).

- 15 G. Coffey, J. Hardy, L. Pedersen, P. Rieke, E. Thomsen, M. Walpole, *Solid State Ionics* **158** 1-9 (2003).
- 16 T. Tsai, S. A. Barnett, *Solid State Ionics* **93** 207-217 (1997).
- 17 S. Wang, Y. Jiang, Y. Zhang, J. Yan, W. Li, *Journal of Electrochemical Society* **145** 1932 (1998).
- 18 B.C.H. Steel, *Solid State Ionics* **86-88** 1223 (1996).
- 19 S. Primdahl, M. Mogensen, *Journal of Electrochemical Society* **145** 2431 (1998).
- 20 S. Yoon, S. Nam, T. Lim, J. Han, S. Hong, *Improved Performance of  $\text{La}_{0.85}\text{Sr}_{0.15}\text{MnO}_3$  cathode by sol-gel coatings*, in Proceedings of the Solid Oxide Fuels VII, Tsurkuba, Ibaraki, 2001, p. 485.
- 21 S. Yoon, J. Han, S. Nam, T. Lim, I. Oh, S. Hong, Y. Yoo, H. Lim, *Journal of Power Sources* **106** 160-166 (2002).
- 22 E. Parry, C.L. Wilson, *Inorganic Chemistry: A Textbook for Advanced Students* Vol. 4 (Longmans Green and Co. 1958).
- 23 X. Huang, J.Liu, Z.Lu, W. Liu, L. Pei, T. He, Z. Liu, W. Su, *Solid State Ionics* **130** 195-201 (2000).
- 24 H. Y. Tu, Y. Takeda, N. Imanishi, O. Yamamoto, *Solid State Ionics* **117** 227 (1999).
- 25 P. Decorse, G. Caboche, L.-C. Dufour, *Solid State Ionics* **117** 161 (1999).
- 26 S. T. Aruna, M. Muthuraman, K.C. Patil, *Solid State Ionics* **120** 275 (1999).
- 27 H. Ullmann, N. Trofimenko, F.Tietz, D. Stöver, A. Ahmad-Khanlou, *Solid State Ionics* **138** 79-90 (2000).
- 28 S. Chaffai, W. Boujelben, M. Ellouze, A. Cheikh-rouhou, J.C. Joubert, *Physica B* **321** 74-78 (2002).
- 29 L. A. Chick, L. R. Pederson, G. D. Maupin, J. L. Bates, L. E. Thomas, G. J. Exarhos, *Materials Letters* **10**, 6-12 (1990).
- 30 G. Coffey, J. Hardy, O. Marina, L. Pedersen, P. Rieke, E. Thomsen, *Copper Doped Lanthanum Strontium Ferrite for Reduced Temperature for Solid Oxide Fuel Cells. Solid State Ionics*, **14** (2003).

- 31 G. Coffey, J. Hardy, L. Pedersen, P. Rieke, E. Thomsen, *Electrochemical and Solid-State Letters*, **6**, 1 (2003).
- 32 I. Kuas, H. Anderson, *Solid State Ionics*, **129** 189 (2000).
- 33 R. Heikes, R. Ure, Jr. *Thermoelectricity: Science and Engineering* (Interscience Publishers 1961).